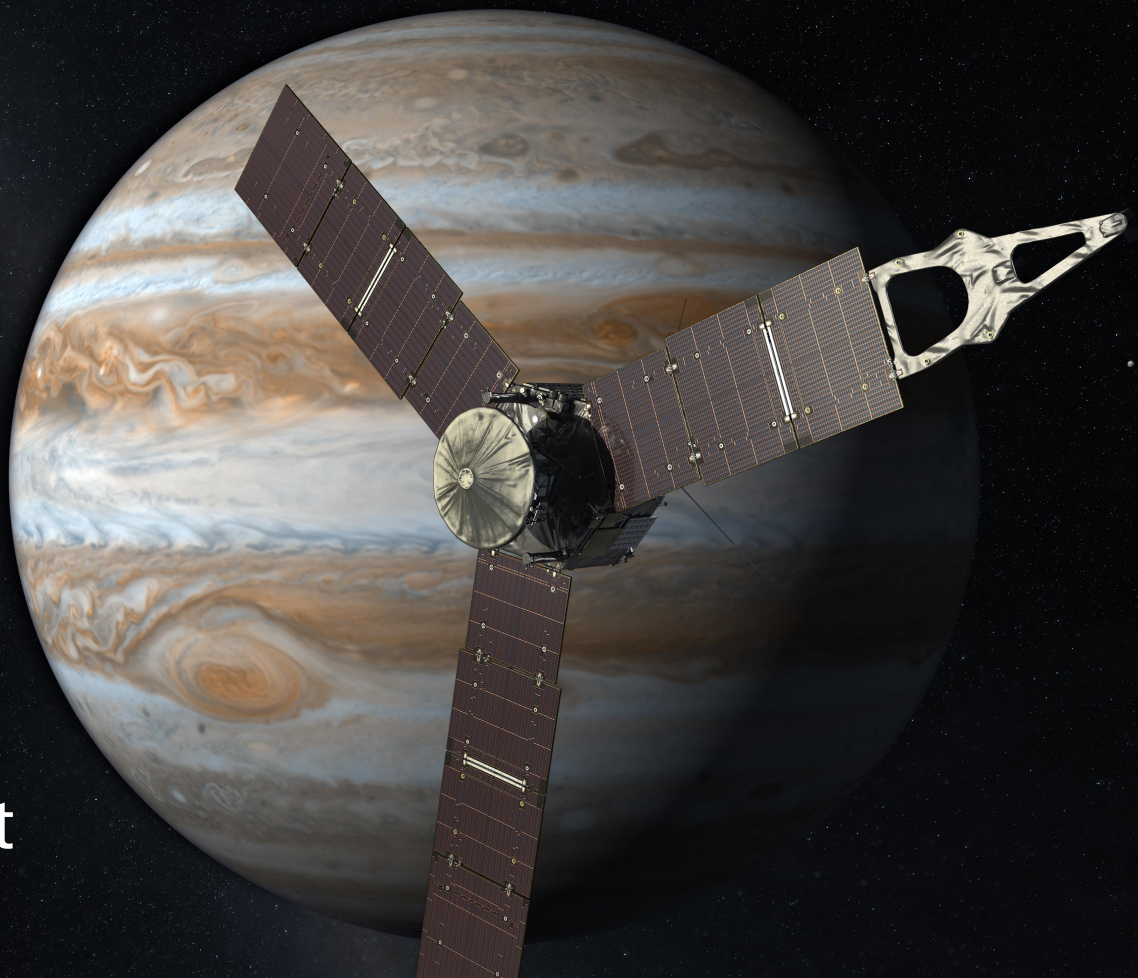


Relativistic Inter- planetary Laser Ranging

J. L. Westin

Master Thesis
Impact of Individual Relativistic Modelling Effects on
Interplanetary Laser Ranging Parameter Estimation



Relativistic Interplanetary Laser Ranging

by

J. L. Westin

to obtain the degree of Master of Science
at Delft University of Technology,
to be defended publicly on Friday July 10, 2020 at 13:00.

Student number:	4283198	
Project duration:	July 2019 – July 2020	
Thesis committee:	Dr. Ir. D. Dirkx,	TU Delft, Supervisor
	Prof. Dr. L. L. A. Vermeersen,	TU Delft, Chair
	Dr. S. Speretta,	TU Delft, External Member

An electronic version of this thesis is available at <http://repository.tudelft.nl/>.

Cover image credit: NASA/JPL, https://www.jpl.nasa.gov/news/press_kits/juno/appendix/.

Acknowledgements

I want to express my thanks to Dominic Dirkx, my daily supervisor for this project. Dr. Dirkx has been helpful and kind throughout the past one and a half years, providing useful advice and giving me motivation to finish the project. I also extend my thanks to Professor Vermeersen and Dr Speretta for being on my defence committee, and helping me round of the project. I also want to thank my family for their support, and for letting me stay rent-free at their house for several decades. Finally, I wish to thank the members of the *Da Vinci Satellite* for giving me something to do when not working on this thesis.

J. L. Westin
Delft, June 26, 2020

Abstract

Interplanetary Laser Ranging (ILR) is an experimental satellite navigation technique with the potential to produce cm- to mm-level accurate and precise range observations over interplanetary distances. This is an improvement over current radio ranging techniques, which can achieve m-level performance. One common application of navigation data is the estimation of physical and astronomical parameters. To utilize the improved observation quality of ILR, it is necessary to use sufficiently detailed observation- and dynamical models during parameter estimation. We investigate the influence of relativistic modelling on parameter estimation quality using ILR data.

Simulated parameter estimation experiments involving a Juno-like Jovian orbiter were used to gauge the impact of 22 different relativistic effects. The spacecraft's initial state, the mass of Jupiter and two post-Newtonian parameters were estimated in each experiment. Parameter estimation error, observation errors and estimation residuals were used as metrics to quantify the influence of each effect. Rough preliminary estimates of an effect's magnitude were found to be a good predictor of the actual impact on estimation error, with some exceptions. Excluding the gravitational influence of Jupiter's velocity and the Jupiter-Sun coupled gravity resulted in almost no change in estimation error, likely due to compensation by the Newtonian gravity term. Similar compensatory relationships can be identified by comparing mean observation errors with mean estimation residuals. Including empirical accelerations in the list of estimated parameters was found to be a good way of reducing parameter estimation error.

List of Symbols and Acronyms

Symbol	Description
\mathbf{a}	Acceleration vector
A_{NC}^{μ}	Non-conservative acceleration tensor
B	Set of celestial bodies
c	Speed of light in vacuum
C_{nm}	Cosine spherical harmonic coefficients
R_{ab}	Retroreflector range observable
$R_{ab}^{(1)}, R_{ab}^{(2)}$	One- and two-way range observables
$g_{\mu\nu} (g^{\mu\nu})$	(Inverse) spacetime metric
G	Gravitational constant
$G_{\mu\nu}$	Einstein curvature
h	Initial state observation model
$h_{\mu\nu}$	Non-Minkowskian metric terms
J_2	Quadrupole moment
M	Mass of a celestial body
\mathcal{O}	Order/Magnitude
p	Detection probability
P_{nm}	Associated Legendre polynomials
r	Receiver
\mathbf{r}	Position vector
R	Range
R	Scalar curvature
$R_{eq,b}$	Equatorial radius of b
$R_{\mu\nu}$	Ricci curvature
s	Spacecraft
t	Transmitter
$\hat{\mathbf{s}}$	Spacecraft orientation vector
S_a	Angular momentum of b
S_{nm}	Sine spherical harmonic coefficients
t	Coordinate time
t_t, t_r	Transmission- and reception time
T	Period
$T_{\mu\nu}$	Stress-energy tensor
$\mathbf{v} (\mathbf{v}_b)$	Velocity vector (of b)
w, w^i	Scalar- and vector relativistic potential
x^{μ}	Spacetime coordinate tensor
x^i	Spatial coordinate tensor
$z (\mathbf{z})$	(Vector of) observations

Symbol	Description
β	PPN nonlinearity parameter
$\eta_{\mu\nu}$	Minkowski metric
δt	Emission delay
δ_{ij}	Kronecker delta tensor
Δ_b	Scalar potential correction term
ϵ_F	Formal error
ϵ_T	True error
ϵ_{TF}	True-to-formal error ratio
γ	PPN rest mass parameter
$\Gamma_{\alpha\beta}^{\mu}$	Christoffel symbol
λ	Longitude
μ	Standard gravitational parameter
ϕ	Latitude
ρ	Mass density
$\rho(\boldsymbol{\rho})$	Residual (vector)
ρ	Range
$\dot{\rho}$	Range rate
$\sigma(\sigma^i)$	mass (current) density
σ	Standard deviation
τ	Proper time

Acronym	Meaning
AU	Astronomical Unit
BCRS	Barycentric Celestial Reference System
CCR	Corner Cube Retroreflector
GR	General Relativity
IAU	International Astronomical Union
ILR	Interplanetary Laser Ranging
LEO	Low Earth Orbit
LLR	Lunar Laser Ranging
PN	Post-Newtonian
PPN	Parametrized Post-Newtonian
SLR	Satellite Laser Ranging
SR	Special Relativity
TTF	Time Transfer Function(s)

Contents

Acknowledgements	iii
Abstract	v
1 Introduction	1
2 Research Paper	3
2.1 Introduction	4
2.2 Interplanetary Laser Ranging	5
2.2.1 Laser Transponder Architecture	5
2.2.2 Current State of ILR	6
2.3 Relativistic Effects.	7
2.3.1 Background	7
2.3.2 Acceleration Effects	9
2.3.3 Light Time Effects	10
2.3.4 Preliminary Estimates	11
2.4 Methodology	12
2.4.1 Environment Definition	12
2.4.2 Experiment Overview	13
2.4.3 Impact Metrics.	15
2.5 Results	16
2.5.1 True-to-Formal Error Ratios	16
2.5.2 Comparison with Mean Observation Error.	17
2.5.3 Observation Errors and Residuals	19
2.6 Discussion	20
2.6.1 Utility of Preliminary Estimates	22
2.6.2 Compensation by Larger Effects	22
2.6.3 Empirical Accelerations	24
2.6.4 Extensions and Generalizations	26
2.7 Conclusions & Recommendations	27
3 Conclusions & Recommendations	35
A Acceleration Model Derivation	37
A.1 Relativistic Equations of Motion	37
A.2 Schwarzschild Term.	39
A.3 Kinetic Term	40
A.4 External Potential Term	40
A.5 Central Body Velocity Term	40
A.6 Central Body Acceleration Term.	41
A.7 Angular Momentum Term	41
A.8 Extrinsic Gravitomagnetic Term.	41
B Model Verification	43
B.1 Acceleration Models	43
B.2 Light Time Models	44
C Integrator Benchmarking	47
C.1 Integrator Selection	47
C.2 Verification	47
Bibliography	49

Introduction

Accurate and precise satellite navigation is a key requirement of almost all space missions. Observations of the spacecraft's position and velocity allow us to estimate not only its state, but also other parameters that affect its motion [21]. The quality of these parameter estimates is partially dependent on the accuracy of the dynamical- and observation models used during the estimation process. In this thesis, we investigate how individual relativistic modelling effects impact the quality of parameter estimates obtained from interplanetary laser ranging (ILR) data.

This thesis is presented in the form of a research paper (Chapter 2) followed by a series of appendices with supplementary information (Appendix A - C). Because it is presented as a stand-alone document, section numbers in the paper omit the chapter number 2 (for example, "Section 2.3" refers to "3. Relativistic Effects"). In the paper, we discuss the simulated experiments that were carried out to assess the impact of relativistic modelling on ILR-based parameter estimates. A brief conclusion of the thesis is given in Chapter 3. Appendix A gives the full derivation of the acceleration effects listed in Section 2.3.2. In Appendix B we present the methods used to verify our acceleration- and observation model software implementations. Finally, our choice of numerical integrator is justified in Appendix C.

Common spacecraft navigation techniques include radio ranging, Doppler tracking, VLBI and laser ranging [33] [25]. VLBI (Very Long Baseline Interferometry) measures the angular position of a radio-emitting spacecraft, while Doppler tracking determines its radial speed (range rate). Radio- and laser-ranging measure the distance (range) to the spacecraft. Laser ranging has historically been more accurate and precise than radio (cm- to mm-level for laser [22] vs. m-level for radio [13]). The limiting factor of retroreflector laser ranging is target distance. Signal attenuation scales with the fourth power of range [7] [22], making laser ranging unfeasible over interplanetary distances. A proposed solution to this problem is given in [7], where a two-way transponder architecture is used to mitigate the attenuation problem. This technique is now known as interplanetary laser ranging (ILR), and is currently undergoing development and testing.

ILR differs conceptually from satellite- and Lunar laser ranging (SLR and LLR) in that the spacecraft is equipped with an active laser emitter instead of retroreflectors. Most ILR mission proposals favour a two-way asynchronous transponder architecture [10, §2.2]. In such a setup, the ground station and spacecraft fire laser pulses independently, and a set of up- and downlink measurements are paired together to mimic a reflected signal pulse. This has the advantage of making the timing stability requirements of the space segment less strict [10, §3.2]. ILR is discussed further in Section 2.2.

A prototype asynchronous laser transponder link with the MESSENGER spacecraft at 24 Gm distance demonstrated that precision of around 20 cm is achievable in practice [29]. Estimates of future ILR performance suggest that cm- to mm-level results could be possible [10] [34]. This increased level of measurement precision (compared to radio ranging) also increases the necessity for accurate modelling. General Relativity (GR), which serves as the modern theory of gravity, introduces various accelerations and light-time effects that need to be accounted for. In this thesis we investigate the impact of each relativistic effect individually, when applied to a parameter estimation using ILR data as its input. The following research question was formulated to describe this goal:

How do individual relativistic modelling effects impact the estimates of spacecraft ephemerides and environmental parameters obtained using ILR observation data?

To fulfil this goal, we ran a series of simulated parameter estimation experiments involving a Jovian orbiter. First, a set of two-way range observations is generated with a noise level of 1 mm. The model used to generate these observations includes all of the identified relativistic effects, and is considered to represent reality in the context of the experiment. These "real" observations are used as an input to a parameter estimation process that uses a separate model, which excludes one relativistic effect. By comparing the outcome of parameter estimation runs where different effects were excluded, we are able to effectively compare the impact of each individual effect. The full experiment method is described in Section 2.4.

We can identify two categories of relativistic modelling effects applicable to our investigation: acceleration- and light time corrections. In addition to relatively large, named effects such as the Shapiro time delay [28] [27] and Schwarzschild acceleration [26, p.156], smaller effects can be derived using generalized methods. With the estimated precision of ILR as a reference, we can identify a collection of relativistic effects that could significantly impact the quality of results derived from ILR observations. Light time correction effects do not need to be considered if their order is significantly lower than the typical observation noise level, which is around 1 cm to 1 mm for ILR. The same condition can be applied to acceleration effects by considering the spacecraft's positional error after one contiguous measurement arc. In Section 2.3 we list the effects that were selected for our investigation, along with preliminary estimates of the observation error caused by each effect.

2

Research Paper

Impact of Relativistic Model Fidelity on Interplanetary Laser Ranging Parameter Estimation Results

Johan Lennart Westin

June 26, 2020

Abstract

Interplanetary Laser Ranging (ILR) is an experimental spacecraft navigation technique with the potential to produce cm- to mm-level range observations over interplanetary distances, a significant improvement over the m-level performance of radio ranging. A common application of navigation data is the estimation of physical and astronomical parameters. To maximize the quality of such parameter estimates, observation- and dynamical models need to be sufficiently detailed. General Relativity introduces several gravitational effects of varying magnitudes that affect both laser pulse propagation and spacecraft dynamics. We investigate the relationship between individual relativistic effects and the resulting parameter estimation quality. This was done through simulated experiments involving a Jovian orbiter. The spacecraft state, mass of Jupiter and two post-Newtonian parameters were estimated using different models, each excluding one relativistic effect to gauge its impact. The parameter error, observation modelling error and estimation residuals were used as figures of merit to quantify the influence of each effect. Rough preliminary estimates of a relativistic effect's magnitude were found to be a good predictor of its relative impact on parameter estimation error, with some exceptions. Exclusion of the gravitational influence of Jupiter's kinetic energy and the Sun-Jupiter coupling from the model only affects the estimate of Jupiter's mass, likely due to compensation by the Newtonian gravity term. Similar compensatory relationships can be identified by comparing pre-estimation observation error to post-estimation residuals. Including empirical accelerations in the list of estimated parameters was found to be a preferable method of compensating for the omitted modelling terms. Overall it is recommended that any ILR parameter estimation effort include all relativistic effects with a magnitude of 0.1 mm or greater, and that empirical accelerations are estimated to compensate for potential modelling errors.

1 Introduction

Accurate and precise satellite navigation is an important part of many space missions. In addition to the direct need for determining a spacecraft's dynamical state, many other parameters such as gravitational fields and physical constants can be estimated from navigation data. Interplanetary Laser Ranging (ILR) as presented in [Degnan, 2002] is an experimental satellite navigation technology with predicted cm- to mm-level precision over interplanetary distances [Turyshev et al., 2010] [Smith et al., 2006]. Its successful implementation could facilitate significant improvements in the estimation of astronomical parameters and physical constants. [Dirkx et al., 2018] identified a number of these parameters, including the Solar oblateness factor J_2 and the relativistic post-Newtonian parameter β . However, this improvement in measurement precision makes the resulting data more susceptible to small modelling errors, such as the exclusion of relativistic effects on spacecraft dynamics and light propagation. In this paper we investigate the impact that a number of such relativistic modelling effects have on the quality of parameter estimation results.

The use of retroreflectors and laser pulses to measure spacecraft- and Lunar range has historically yielded cm- to mm-level accurate ranging results [Murphy, 2013] [Pearlman et al., 2002]. Signal attenuation is the limiting factor preventing laser ranging from being utilized over interplanetary distances. [Degnan, 2002] proposes a solution to this problem by combining concepts from laser ranging and radio transponder setups. An ILR link consists of the ground- and space segments both firing laser pulses at one another asynchronously, with pairs of successful detections being reconstructed into a two-way range measurement [Dirkx et al., 2018]. ILR is discussed in more detail in Section 2.

The theory of General Relativity shows that light does not necessarily move in straight Euclidean paths [Hartle, 2003, p.178, 179]. The largest relativistic effect on light time is that presented in [Shapiro, 1964]. Additional analytical terms and general expressions for this light time delay are derived in e.g. [Teyssandier and le Poncin-Lafitte, 2008] and [Hees et al., 2014]. General relativity also affects the orbit of the spacecraft or celestial body being tracked [Kopeikin et al., 2011] [Dirkx et al., 2015]. We investigate the influence of individual relativistic effects, both as they affect laser pulse propagation and spacecraft dynamics, on orbit determination results using ILR observations. The full list of effects we study is given in Section 3.

The central feature of ILR is the prospect of high-precision range observations over large distances. Whereas traditional retroreflector ranging becomes unfeasible beyond the Moon, ILR remains a viable alternative for ranging to the outer planets. A theoretical study on the scientific utility of ILR was conducted in [Dirkx et al., 2018]. This investigation concluded that Solar system parameters with a long-periodic influence on spacecraft motion could be estimated more accurately with the high precision range data offered by ILR. In our investigation, we simulate the parameter estimation process for a Jovian orbiter in a highly elliptical orbit (See Section 4).

In order to gauge the impact of relativistic modelling effects on parameter estimation results, a series of simulated experiments were carried out. In each experiment, the parameter estimation process is run using a model that excludes a single relativistic effect. The resulting parameter estimation errors are then compared. The methodology for the experiment is discussed further in Section 4. The outcome of these experiments is presented in Section 5.

With this research we aim to establish the relationship between relativistic modelling error and parameter estimation quality. Determining the connection between these two factors should aid making the construction of relativistic models for real ILR studies more efficient. Using preliminary estimates and the results of our simulated experiments, it is possible to formulate a straightforward criterion to determine whether a relativistic effect is worth including in the estimation model. If the estimated magnitude of an effect, determined before parameter estimation, is lower than the observation noise level, it can be safely excluded from the estimation model without significantly impacting parameter error. We also investigated the ways in which different modelling effects compensate for one another, and how this effect can be achieved more consistently using empirical accelerations. These topics are discussed in detail in Section 6. Finally, Section 7 provides a summary of our conclusions and makes recommendations for further research on this topic.

2 Interplanetary Laser Ranging

Interplanetary Laser Ranging (ILR) was first proposed by [Degnan, 2002] as a way to extend the functionality of current laser ranging methods to interplanetary missions. It combines the two-way transponder architecture typical to radio-based systems with the use of laser pulse emitters and receivers. ILR is expected to provide range measurements with cm- to mm-level precision and accuracy over interplanetary distances [Turyshv et al., 2010] [Dirkx et al., 2018]. The technology has been successfully demonstrated with the MESSENGER spacecraft at 24 Mm distance [Smith et al.,

2006]. In this section we cover the details of the ILR architecture, its current state of development and its role in our experiment.

2.1 Laser Transponder Architecture

Most modern laser ranging setups use corner-cube retroreflectors (CCRs) to efficiently reflect signals off the target spacecraft back to the original transmission source. Given a time Δt between sending and receiving a laser pulse, the range R from the ground station to spacecraft is roughly $c\Delta t/2$. Laser ranging is typically divided into the categories of *satellite laser ranging* (SLR) for Earth orbiting spacecraft, and *Lunar laser ranging* (LLR) for tracking the Moon’s surface. These techniques have historically yielded very accurate (cm- to mm-level) tracking results of near-Earth spacecraft [Pearlman et al., 2002] and similar performance for tracking the Lunar surface [Murphy, 2013].

In CCR-based laser ranging, the attenuation of the original signal is proportional to R^4 [Degnan, 2002]. This makes the use of CCRs feasible at near-Earth and Lunar distances [Murphy, 2013], but becomes impractical for interplanetary targets due to the rarity of successfully detected return signals. The laser transponder architecture aims to remedy this limitation.

An active two-way laser transponder system requires both observers to have laser emission and detection hardware installed. Such equipment is available on Earth in the form dozens of laser ranging stations [Pearlman et al., 2002]. Recent developments in laser time transfer (LTT) and laser communication could serve as incentives to develop sufficiently powerful laser hardware for spacecraft to facilitate effective ILR implementations [Dirkx et al., 2018]. Current ILR demonstrators such as that in [Smith et al., 2006] make use of a spacecraft’s laser altimeter, which is not designed specifically for ILR applications. The use of purpose-built hardware could improve the achievable ILR performance over the current demonstrators.

There are two main transponder types, namely *echo* and *asynchronous* [Degnan, 2002]. In the case of an echo transponder, the space segment waits for pulses to arrive from the ground station and sends a response back after some delay δt . An asynchronous transponder setup has both observers firing pulses constantly, with little or no explicit coordination. A pair of successful detections is then selected such that they emulate an echo transponder observation. The delay δt can have different values, including being negative. It is also generally much larger than for an echo transponder. Figure 1 shows how the delay times differ between echo- and asynchronous transponders.

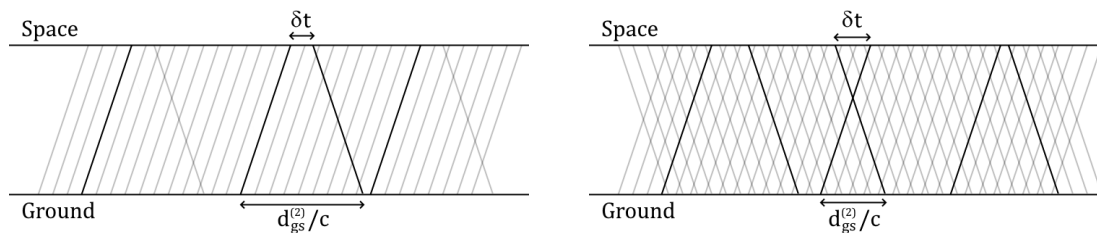


Figure 1: Example observations for the echo- (Left) and asynchronous (Right) transponder setups. Black lines indicate successful detections while gray lines represent pulse transmissions. Notice the larger number of successful two-way observations in the asynchronous case (3 vs 1). An example of negative δt is highlighted.

The main advantage of asynchronous transponders over the echo architecture is the amount of data that can be produced. Assuming operation in the single-photon domain, each emitted pulse has a probability $p \ll 1$ of being detectable at the other end of the link. For an echo transponder, each pulse that is successfully detected in the uplink has to go through the same process in the

downlink. This effectively reduces the probability of a given pulse producing a successful reading to p^2 . Downlink emissions will also be triggered upon noise detections matching the calibrated laser wavelength. The asynchronous transponder setup differs only in the fact that downlink pulses are sent continuously, instead of in response to successful uplink detections. This increases the volume of successful uplink- and downlink observations to p instead of p^2 . For low-power and/or long-distance links where p is low, this difference can become very significant.

For a given two-way observation between two observers a and b there are four relevant moments in time: The initial transmission time $t_{t,a}$, reception $t_{r,b}$, retransmission time $t_{t,b} = t_{r,b} + \delta t$ and the final reception time $t_{r,a}$. The two-way range observable $R_{ab}^{(2)}$ then becomes: [Dirx et al., 2018]

$$R_{ab}^{(2)} = R_{ab}^{(1)}(t_{t,a}, t_{r,b}) + c\delta t + R_{ba}^{(1)}(t_{t,b}, t_{r,a}) \quad (1)$$

where $R_{ab}^{(1)}$ is a one-way range observation between observers p and q given by:

$$R_{pq}^{(1)}(t_{t,p}, t_{r,q}) = |\mathbf{r}_q(t_{r,q}) - \mathbf{r}_p(t_{t,p})| + \Delta R_{pq}(t_{t,p}, t_{r,q}) \quad (2)$$

Here $\mathbf{r}_x(t)$ is the position of observer x at time t , and $\Delta R(t_a, t_b)$ encompasses all higher-order effects, errors and noise terms. Investigating the impact of these higher-order observation effects (specifically those caused by relativity) is one of the goals of our experiment (see Section 3).

2.2 Current State of ILR

Several experiments have been carried out to demonstrate the feasibility of non-CCR ranging to spacecraft. One-way laser links have been used to conduct laser ranging to the Hayabusa2 spacecraft [Noda et al., 2017] and the Lunar Reconnaissance Orbiter [Bauer et al., 2017] [Bauer, 2017]. Two-way asynchronous laser transponder links have been established with the MESSENGER spacecraft on two different days during calibration of its laser altimeter. These experiments demonstrated a range agreement with radio measurements within 52 m, an estimated precision of ± 20 cm [Smith et al., 2006]. As the technology matures, this performance could likely be improved to the predicted cm- to mm level. [Turyshev et al., 2010]

The overall expected performance of ILR is similar to current SLR and LLR results. A comprehensive list of error sources was made in [Dirx et al., 2018, §3]. The main identified sources of error were detector- and pulse width uncertainty, systematic errors from hardware imperfections, and instabilities (i.e. random walk behaviour) from tropospheric influences and ground station positioning. Based on random uncertainties from the detectors and laser pulse width, precision between 1 and 4 mm was estimated to be achievable by averaging over 10 measurements. Increasing the number of measurements could reduce this to less than 0.1 mm. Hardware imperfections create systematic errors on the order of several mm, based on figures from SLR. Random-walk error sources limit the achievable accuracy of ILR to just below the cm level. Modelling of these unstable error sources are fields of active research, and may improve achievable ILR performance in the future. In our study, we use a simple Gaussian noise model with a standard deviation of 1 mm.

3 Relativistic Effects

The relativistic effects we study fall into two categories: acceleration- and light time effects. The former influences the spacecraft motion, while the latter affects the observed propagation time of laser pulses between targets. In this section we provide some background on the how these relativistic effects can be derived (Section 3.1), as well as a list of effects that we will study (Sections 3.2 and

3.3). We also provide some preliminary estimates of the magnitude of each effect in 3.4. These estimates are later discussed in Section 6.1 as a potential metric for filtering out negligible effects during the construction of a relativistic model.

3.1 Background

The General Theory of Relativity (GR) describes how the curvature of four-dimensional spacetime affects the behaviour of matter and light within it. The relationship between spacetime curvature $R_{\mu\nu}$ and energy-, mass- and momentum density $T_{\mu\nu}$ is summarized by the Einstein equation: [Hartle, 2003, p.483]

$$R_{\mu\nu} - \frac{1}{2}Rg_{\mu\nu} = 8\pi GT_{\mu\nu} \quad (3)$$

where $R_{\mu\nu}$ is the Ricci curvature tensor, R is its trace, $T_{\mu\nu}$ is the stress-energy tensor, $g_{\mu\nu}$ is the spacetime metric tensor and G is the gravitational constant. Out of these, the metric tensor is relevant for deriving the relativistic effects used in our simulations. We express the metric as a linear combination $g_{\mu\nu} = \eta_{\mu\nu} + h_{\mu\nu}$, where $\eta_{\mu\nu} = \text{diag}(-1, 1, 1, 1)$. This is a common simplification called *linearized gravity*, which simplifies the analysis of the highly non-linear Einstein equation given above [Hartle, 2003, p.459]. $\eta_{\mu\nu}$ is called the Minkowski metric, and corresponds to a flat spacetime model. $h_{\mu\nu}$ is called the metric perturbation, and can be the non-flat component of the metric. In our analysis, we use a formulation of $h_{\mu\nu}$ based on the IAU recommendations [Soffel et al., 2003]: [Dirkx et al., 2015] [Will, 1971] [Ni, 1972]

$$\begin{aligned} h_{00} &= \frac{2w}{c^2} - \frac{2\beta w^2}{c^4} + \mathcal{O}(c^{-5}) \\ h_{0i} &= -(\gamma + 1)\frac{2w^i}{c^3} + \mathcal{O}(c^{-5}) \\ h_{ij} &= \delta_{ij}\frac{2\gamma w}{c^2} + \mathcal{O}(c^{-4}) \end{aligned} \quad (4)$$

where w and w^i are the scalar- and vector potentials, respectively, c is the speed of light and $\delta_{\mu\nu} = \text{diag}(1, 1, 1, 1)$ is the Kronecker delta tensor. This metric is a parameterized post-Newtonian (PPN) variant of the IAU 2000 recommendation [Soffel et al., 2003]. It includes two post-Newtonian parameters, namely the rest mass curvature parameter γ and the superposition non-linearity parameter β [Misner et al., 1973, p.1072]. Both have a value of 1 in GR, and have been experimentally confirmed to be within 10^{-5} of this value [Bertotti et al., 2003]. [Dirkx et al., 2018] identifies these parameters as having potential to get improved estimates as a result of ILR. For this reason, we include these as two of the estimated parameters in our simulations.

For the potentials w and w^i we use the expressions given by [Soffel et al., 2003], namely:

$$w_b = w_{0,b} - \frac{\Delta w_b}{c^2} \quad \text{where} \quad \Delta w_b = \frac{\mu_b}{r_b} \left(-2v_b^2 + \sum_{a \neq b} w_{0,a} + \frac{(\mathbf{v}_b \cdot \mathbf{r}_b)^2}{2r_b^2} + \frac{\mathbf{a}_b \cdot \mathbf{r}_b}{2} \right) \quad (5)$$

$$w_b^i = -\frac{G(\mathbf{S}_b \times \mathbf{r}_b)^i}{2r_b^3} + w_{0,b}v_b^i \quad (6)$$

where b is some body with mass $M_b = \mu_b/G$, angular momentum S_b , speed v_b etc. Here $w_{0,b}$ is the point-mass potential μ_b/r_b (we ignore spherical harmonics in our analysis, except in the J_2 light

time effect, see Equation 22). The external potential term $\sum_{a \neq b} w_{0,a}$ includes all bodies in the environment other than b , but in practice will typically only consider the Sun. Furthermore, note that \mathbf{r}_b is the position of the observer w.r.t. b , not of b w.r.t. the Solar system barycenter.

With this expression for the metric $g_{\mu\nu}$, the acceleration effects can be derived using the geodesic equation. This expression describes the world line of an object as a function of the metric $h_{\mu\nu}$ through the Christoffel symbols $\Gamma_{\alpha\beta}^{\mu}$: [Hartle, 2003] [Dirkx et al., 2015]

$$\frac{d^2 x^{\mu}}{d\tau^2} = -\Gamma_{\alpha\beta}^{\mu} \frac{dx^{\alpha}}{d\tau} \frac{dx^{\beta}}{d\tau} \quad \text{where} \quad \Gamma_{\alpha\beta}^{\mu} = \frac{1}{2} g^{\mu\nu} \left(\frac{\partial h_{\nu\alpha}}{\partial x^{\beta}} + \frac{\partial h_{\nu\beta}}{\partial x^{\alpha}} - \frac{\partial h_{\alpha\beta}}{\partial x^{\nu}} \right) \quad (7)$$

It is more convenient for us to express the above dynamical equation in terms of the coordinate time t instead of proper time τ . For this we can use the following expression: [Kopeikin et al., 2011]

$$\frac{d^2 x^i}{dt^2} = -c^2 \Gamma_{00}^i - 2c \Gamma_{0j}^i \frac{dx^j}{dt} - \Gamma_{jk}^i \frac{dx^j}{dt} \frac{dx^k}{dt} + \frac{dx^i}{dt} \left(c \Gamma_{00}^0 + 2 \Gamma_{0j}^0 \frac{dx^j}{dt} + \frac{1}{c} \Gamma_{jk}^0 \frac{dx^j}{dt} \frac{dx^k}{dt} \right) \quad (8)$$

Here x^i is the tensor equivalent of the spacecraft's position vector \mathbf{r}_b . x^i represents three coordinates, x^1 , x^2 and x^3 , which are equivalent to the x -, y - and z -components of \mathbf{r}_b . Finally, by expanding the Christoffel symbols Γ_{00}^i , Γ_{0j}^i etc. explicitly using the metric in Equation 4 [Kopeikin et al., 2011] [Dirkx et al., 2015], we get the following equations of motion in terms of the potentials w and w^i :

$$\begin{aligned} \ddot{x}^i = w_{,i} + \frac{1}{c^2} [& \dot{x}^j \dot{x}^k \gamma (\delta_{jk} w_{,i} - \delta_{ij} w_{,k} - \delta_{ik} w_{,j}) - 2(\gamma + \beta) w \cdot w_{,i} - \dots \\ & \dots - 2\dot{x}^i \dot{x}^j w_{,j} + 2(\gamma + 1) \dot{x}^j (w_{,j}^i - w_{,i}^j)] + \mathcal{O}(c^{-3}) \end{aligned} \quad (9)$$

Here the $,i$ subscript is shorthand for $\partial/\partial x^i$. Our formulation of the relativistic potential assumes that factors such as planetary mass and angular momentum remain constant over time. Because our potential does not explicitly depend on time, all time-derivative terms that would otherwise appear have been omitted.

In the following section presents the acceleration effects that were derived using this dynamical framework. Each effect is obtained by substituting a single term from the potential (Equations 5 and 6) into Equation 9. We also split the equations of motion into three distinct parts as follows:

$$\begin{aligned} \ddot{x}_{\text{first order}}^i &= w_{,i} \\ \ddot{x}_{\text{Schwarzschild}}^i &= \frac{1}{c^2} [\dot{x}^j \dot{x}^k \gamma (\delta_{jk} w_{,i} - \delta_{ij} w_{,k} - \delta_{ik} w_{,j}) - 2(\gamma + \beta) w \cdot w_{,i} - 2\dot{x}^i \dot{x}^j w_{,j}] \\ \ddot{x}_{\text{vector}}^i &= \frac{2(\gamma + 1)}{c^2} \dot{x}^j (w_{,j}^i - w_{,i}^j) \end{aligned} \quad (10)$$

The above discussion applies to the derivation of acceleration effects. In addition to this, we also consider relativistic light time effect that influence our observations. The largest relativistic light time effect was first shown in [Shapiro, 1964]. Various methods have been developed to compute light time delay more generally, either numerically or analytically. One such method is the direct numerical integration of the geodesic equation, which governs relativistic light propagation (See Equation 7) [Blanchet et al., 2001]. This method becomes very computationally intensive when

dealing with higher-order relativistic effects, even in a static, spherically symmetric spacetime formulations [Teyssandier and le Poncin-Lafitte, 2008, §1]. It is also difficult to distinguish individual relativistic effects using this approach, making it non-ideal for our application.

Two alternative methods for computing relativistic light time effects analytically are the *world function* and the *time transfer function* (TTF). The Synge world function was first given in [Synge, 1931] and is defined as half of the squared geodesic distance between two points. A general expansion of the world function to arbitrary order was presented in [le Poncin-Lafitte et al., 2004]. The TTF simply measures the difference in coordinate time between two events. A third-order approximation was given in [le Poncin-Lafitte et al., 2004, §5], and an expansion up to arbitrary order in [Teyssandier and le Poncin-Lafitte, 2008]. Analytical formulae for several relativistic light time effects were derived in [Hees et al., 2014], three of which are used in this experiment (See Section 3.3).

To give an idea of how these light time effects were derived, the following formulation is given in [Teyssandier and le Poncin-Lafitte, 2008] for the first-order one-way light time correction term:

$$\Delta R = \frac{1}{2}R \int_0^1 \left[g_{(1)}^{00} - N^i g_{(1)}^{0i} + N^i N^j g_{(1)}^{ij} \right]_{z(\mu)} d\mu \quad (11)$$

Here ΔR is the light time correction with respect to a nominal range estimate R . N^k is a normalized (length 1) oriented parallel to propagation path of the light signal. $g_{(1)}^{\mu\nu}$ is the first-order terms of the spacetime metric. $z(\mu)$ is a linear parametrisation of the space between the emitter \mathbf{x}_e and receiver \mathbf{x}_r . That is, $z(0) = \mathbf{x}_e$ and $z(1) = \mathbf{x}_r$, with all the values in between lying on the light travel path.

At a high level, we can interpret Equation 11 as a summation of the influence that spacetime curvature has on light time over the entire travel path of the signal. An integration is carried out starting at the emitter (e.g. ground station) and ending at the receiver (e.g. spacecraft), with each point on the intermediate path providing a contribution dependent on the local spacetime curvature $g_{(1)}^{\mu\nu}$. A crucial distinction between light time effects and accelerations is that the former is dependent on the value of the spacetime metric at all points along the light propagation path, while the latter is only influenced by $g_{\mu\nu}$'s value at the affected body's position (i.e. at the spacecraft).

[Teyssandier and le Poncin-Lafitte, 2008] gives a detailed framework for deriving light time corrections up to an any degree. While we have chosen to derive most of the acceleration effects given below ourselves, the light time effects are taken from literature. Specifically, we have selected four light time delay contributions from [Teyssandier and le Poncin-Lafitte, 2008] and [Hees et al., 2014], based on their approximate magnitude compared to the our observation noise level of 1 mm.

3.2 Acceleration Effects

Using the method described above, seven relativistic acceleration effects were derived. These are in addition to the classical point-mass gravity term:

$$\mathbf{a}_{\text{pmg}} = -\frac{\mu_b}{r_b^3} \mathbf{r}_b \quad (12)$$

This term is obtained by substituting w_0 into $\ddot{x}_{\text{first order}}$ in Equation 10. Because this term is large and cannot be excluded from any experiments, we do not study this acceleration component as a relativistic effect.

The Schwarzschild acceleration is obtained by substituting $w_0 = \mu_b/r_b$ into $\ddot{x}_{\text{Schwarzschild}}^i$:

$$\mathbf{a}_{\text{sch}} = \frac{\mu_b}{r_b^3 c^2} \left[\left(2(\gamma + \beta) \frac{\mu_b}{r_b} - \gamma v^2 \right) \mathbf{r}_b + 2(1 + \gamma)(\mathbf{r}_b \cdot \mathbf{v}) \mathbf{v} \right] \quad (13)$$

For the next four effects, we take the terms in $\Delta w_b/c^2$ and substitute them into $\ddot{x}_{\text{first order}}^i$. We do not derive their Schwarzschild-equivalents ($\Delta w_b/c^2 \rightarrow \ddot{x}_{\text{Schwarzschild}}^i$) as these are of order $\mathcal{O}(c^{-4})$.

The first of these potential terms is $w_{\text{kin}} = 2\mu_b v_b^2/r_b c^2$. We call this the *kinetic potential* as it is proportional to the kinetic energy of the central body b . Substituting this into $\ddot{x}_{\text{first order}}^i$ produces the following acceleration:

$$\mathbf{a}_{\text{kin}} = -\frac{2\mu_b v_b^2}{r_b^3 c^2} \mathbf{r}_b \quad (14)$$

Notice that this term is proportional to the point-mass gravity ($\mathbf{a}_{\text{kin}} = 2(v_b/c)^2 \mathbf{a}_{\text{pmg}}$).

Next, we use the potential due to external bodies, $w_{\text{ext}} = -\sum_{a \neq b} \mu_b \mu_a / r_b r_{ab} c^2$. Here r_{ab} is the position of b with respect to a , where a is called the *primary body*. The external potential acceleration due to a single primary body a is given by:

$$\mathbf{a}_{\text{ext}} = \frac{\mu_b \mu_a}{r_b^3 c^2 r_{ab}} \mathbf{r}_b \quad (15)$$

Again, notice that $\mathbf{a}_{\text{ext}} \propto \mathbf{a}_{\text{pmg}}$. The next effect is dependent on the velocity of b , and we call it the *central body velocity* term. The potential $w_{\text{cbv}} = \mu_b (\mathbf{v}_b \cdot \mathbf{r}_b)^2 / 2r_b^3 c^2$ results in the following acceleration:

$$\mathbf{a}_{\text{cbv}} = \frac{\mu_b}{r_b^3 c^2} \cdot \frac{\mathbf{v}_b \cdot \mathbf{r}_b}{2} \left[3 \frac{\mathbf{v}_b \cdot \mathbf{r}_b}{r_b^2} \mathbf{r}_b - 2\mathbf{v}_b \right] \quad (16)$$

Similarly, the *central body acceleration* term is dependent on the acceleration of b . The potential $w_{\text{cba}} = \mu_b (\mathbf{a}_b \cdot \mathbf{r}_b) / 2r_b c^2$ produces the following acceleration:

$$\mathbf{a}_{\text{cba}} = \frac{\mu_b}{2r_b c^2} \left[\frac{\mathbf{a}_b \cdot \mathbf{r}_b}{r_b^2} \mathbf{r}_b - \mathbf{a}_b \right] \quad (17)$$

The final two acceleration terms come from the vector potential w^i (Equation 6). These are called *gravitomagnetic* effects by e.g. [Kopeikin, 2010]. The angular momentum term is also commonly known as the *Lense-Thirring* effect. It is based on the potential term $w_{\text{ang}}^i = G(\mathbf{S}_b \times \mathbf{r}_b)^i / 2r_b^3$, which we substitute into $\ddot{x}_{\text{vector}}^i$ (See Equation 10). The resulting expression is: [Petit and Luzum, 2010]

$$\mathbf{a}_{\text{ang}} = \frac{\mu_b}{r_b^3 c^2} \cdot (\gamma + 1) \left[\frac{3(\mathbf{r}_b \cdot \mathbf{J}_b)}{r_b^2} (\mathbf{r}_b \times \mathbf{v}) + \mathbf{v} \times \mathbf{J}_b \right] \quad (18)$$

where $\mathbf{J}_b = \mathbf{S}_b / M_b$ is the specific angular momentum. Note that \mathbf{v} is the velocity of the spacecraft, not the central body.

The final effect is the *extrinsic gravitomagnetic* acceleration, obtained from the potential $w_{\text{xgm}}^i = \mu_b v_b^i / r_b$. Its expression is:

$$\mathbf{a}_{\text{xgm}} = \frac{\mu_b}{r_b^3 c^2} \cdot 2(\gamma + 1) ((\mathbf{v}_b \cdot \mathbf{v}) \mathbf{r}_b - (\mathbf{r}_b \cdot \mathbf{v}) \mathbf{v}_b) \quad (19)$$

3.3 Light Time Effects

Light time effects are the second class of relativistic corrections we consider. These are part of the ILR observation model. As described in Section 2, ILR observations are made by recording four points in time when laser pulses are emitted and received. Spacetime curvature causes photons to (appear to) travel along curved trajectories, making the first-order approximation $R = c\Delta t$ inaccurate. These inaccuracies can be compensated for by including the appropriate relativistic light time corrections in our model. Below is a description of the four light time effects used in our simulated experiments.

[Shapiro, 1964] presented the first-order contribution of a single static mass monopole to light time delay. This effect is now called *Shapiro time delay* after the author and is the largest contribution to the relativistic light time correction. Each body that gravitationally influences the light pulse contributes to the total light time correction. The formulation below, as given in e.g. [Teysandier and le Poncin-Lafitte, 2008, p.11] is expressed in terms of the distances R , r_{bt} and r_{br} , where b is the central body and t , r are the transmitter and receiver, respectively.

$$\Delta R_{\text{shp}} = \frac{(1 + \gamma)\mu_b}{c^2} \ln \left(\frac{r_{bt} + r_{br} + R}{r_{bt} + r_{br} - R} \right) \quad (20)$$

Here γ is the post-Newtonian parameter introduced in Section 3.1. Shapiro time delay can be around $\mathcal{O}(10 \text{ km})$ due to the Sun and $\mathcal{O}(10 \text{ m})$ from to Jupiter [Hees et al., 2014]. The Earth also contributes around $\mathcal{O}(10 \text{ cm})$ (See e.g. Figure 6).

The second-order light time correction due to a static mass monopole is given by: [Teysandier and le Poncin-Lafitte, 2008, p.11]

$$\Delta R_{\text{2nd}} = \frac{\mu_b^2}{c^4} \cdot \frac{R}{r_{bt}r_{br}} \left[\frac{(8 - 4\beta + 8\gamma + 3\delta) \arccos(D)}{4\sqrt{1 - D^2}} - \frac{(1 + \gamma)^2}{1 + D} \right] \quad (21)$$

where $D = \hat{\mathbf{r}}_{bt} \cdot \hat{\mathbf{r}}_{br}$ and δ is an additional PPN parameter. In our analysis we will assume $\delta = 1$.

General expressions for the contribution of the zero-order spherical harmonic terms J_n are derived in [Hees et al., 2014]. For our experiment we will only consider the contribution of equatorial oblateness, J_2 . The light time correction due to J_2 is given by: [Hees et al., 2014, p.10]

$$\Delta R_{J_2} = \frac{\mu_b}{c^2} \cdot \frac{J_{2,b} R_{eq,b}^2}{r_{bt}r_{br}} \cdot \frac{R}{1 + D} \times \left[\frac{1 - K_t^2}{r_{bt}} + \frac{1 - K_r^2}{r_{br}} - \left(\frac{1}{r_{bt}} + \frac{1}{r_{br}} \right) \frac{(K_t + K_r)^2}{1 + D} \right] \quad (22)$$

where $K_t = \hat{\mathbf{k}} \cdot \hat{\mathbf{r}}_{bt}$ and $K_r = \hat{\mathbf{k}} \cdot \hat{\mathbf{r}}_{br}$, with $\hat{\mathbf{k}}$ being the central body's axis of symmetry. Here R_{eq} is the reference equatorial radius of the body producing the effect, and $\hat{\mathbf{k}}$ is a unit vector indicating the orientation of the body's axis of symmetry. This light time delay contribution is heavily dependent on the observers' positions with respect to the perturbing body. The effect is largest when $D \approx -1$, i.e. when \mathbf{r}_{bt} and \mathbf{r}_{br} are close to antiparallel. This occurs when the observers are on opposite sides of the perturbing body and the ray of light passes close to its surface. This property is also true for the second-order static mass monopole contribution given in Equation 21.

The final light time effect we consider is that caused by the motion of a central body with velocity \mathbf{v}_b : [Hees et al., 2014]

$$\begin{aligned}
\Delta R_{\text{vlt}} = & \frac{(1 + \gamma)\mu_b}{c^3} \left[\mathbf{v}_b \cdot \hat{\mathbf{R}} \ln \left(\frac{r_{bt} + r_{br} + R}{r_{bt} + r_{br} - R} \right) + \dots \right. \\
& \dots + \frac{2R}{(r_{bt} + r_{br})^2 - R^2} (c(t_r - t_0) \mathbf{v}_b \cdot (\hat{\mathbf{r}}_{bt} + \hat{\mathbf{r}}_{br}) - \dots \\
& \left. \dots - (r_{bt} + r_{br}) \hat{\mathbf{R}} \cdot \mathbf{v}_b - R \hat{\mathbf{r}}_{bt} \cdot \mathbf{v}_b \right] \tag{23}
\end{aligned}$$

Here time t_0 is some reference time at which the perturbing body's state is known. The light time correction given above assumes the perturbing body's motion to be uniform, in which case the choice of t_0 is arbitrary. However, because real Solar system bodies move with non-uniform velocity, it becomes necessary to select t_0 such that the error caused by this approximation is as small as possible. The following formula can be used to select the optimal t_0 : [Hees et al., 2014, p.8]

$$t_0 = \max \left(t_t, t_r - \max \left(0, \frac{\mathbf{g} \cdot (\mathbf{r}_{br}(t_r))}{c|\mathbf{g}|^2} \right) \right) \tag{24}$$

where $\mathbf{g} = \hat{\mathbf{R}} - \mathbf{v}_b(t_r)/c$. The value of t_0 is guaranteed to lie between the reception- and emission times t_t and t_r . Finally, note that the observer positions r_{bt} and r_{br} in Equation 23 are defined with respect to the perturbing body's position at time t_0 .

3.4 Preliminary Estimates

Tables 2 and 3 provide a summary of the relativistic effects discussed above. The given abbreviations ("sch", "kin", "shp" etc.) are used in the following sections. We use the shorthand [B,abr] to denote the effect with abbreviation "abr" caused by body B, where we use S, J and E the Sun, Jupiter and Earth, respectively. For example, [S,xgm] represents the extrinsic gravitomagnetic acceleration effect caused by the Sun.

Preliminary estimates for the effects are also given. The approximation formulae for the accelerations are based on Equations 13 to 19. All vector quantities were replaced with their scalar equivalents, and all signs made positive. For example, in Equation 17 we convert $(\mathbf{a}_b \cdot \mathbf{r}_b) \mathbf{r}_b / r_b - \mathbf{a}_b$ into $a_b r_b^2 / r_b^2 + a_b = 2a_b$. This yields conservative (i.e. large) estimates.

The acceleration magnitudes are expressed as a multiple of $a_{\text{pmg}} \approx 20 \text{ m/s}^2$. Assuming constant linear acceleration over an entire 12-hour integration arc (See Section 4.1) the total displacement error Δs can be conservatively estimated by $\Delta s = \Delta a t^2 / 2$. Using $t = 12 \text{ hrs} = 43,200 \text{ s}$ and setting $\Delta s = 10^{-3} \text{ m}$ based on the ILR noise level, we can conclude that accelerations below $a = 2\Delta s / t^2 \approx 10^{-12} \text{ m/s}^2$ are extremely unlikely to influence the results at all. Based on this, [S,cb] and [J,cb] are not modelled in our simulation. Some of the remaining effects ended up having little to no influence on our results, and these are discussed further in Section 5.

Name	Value	Formula	Name	Value	Formula
μ_J	$1.3 \times 10^{17} \text{ m}^3/\text{s}^2$	GM_J	μ_S	$1.3 \times 10^{20} \text{ m}^3/\text{s}^2$	GM_S
J_J	$3.6 \times 10^{11} \text{ m}^2/\text{s}$	S_J/M_J	c	$3 \times 10^8 \text{ m/s}$	-
r_J	$7.6 \times 10^7 \text{ m}$	$r_{J,p}$	r_{SJ}	$7.8 \times 10^{11} \text{ m}$	-
v_J	$1.2 \times 10^4 \text{ m/s}$	$\sqrt{\mu_S/r_{SJ}}$	v	$7.1 \times 10^4 \text{ m/s}$	$v_J + \sqrt{\mu_J(2/r_{J,p} - 1/a)}$
a_J	$2.1 \times 10^{-4} \text{ m/s}^2$	μ_S/r_{SJ}^2			

Table 1: Values used for the approximations given in Table 2. Values of G, c, M_J, M_S, r_{SJ} are from [Lissauer and de Pater, 2017], and S_J taken from [Soffel et al., 2003, p.2704].

Name		Approximation	Magnitude (J)	Modelled	Studied
Point Mass Gravity	pmg	-	1	S, J	-
Schwarzschild	sch	$(2\mu_J/r_J + 5v^2)/c^2$	10^{-5}	S, J	S, J
Kinetic	kin	$2v_J^2/c^2$	10^{-9}	S, J	S, J
External Potential	ext	$\mu_S/r_{SJ}c^2$	10^{-9}	J	J
Central Body Velocity	cbv	$5v_J^2/2c^2$	10^{-9}	S, J	S, J
Central Body Acceleration	cba	a_{JR_J}/c^2	10^{-13}	-	-
Angular Momentum	ang	$8v_{J_J}/r_Jc^2$	10^{-8}	S, J	S, J
Extrinsic Gravitomagnetic	xgm	$4v_Jv/c^2$	10^{-8}	S, J	S, J

Table 2: Summary of relativistic acceleration effects considered in the experiment. Approximations are given relative to the point-mass gravity (pmg) term, and only computed for Jupiter. Effects in the "Modelled" column are included in the truth model (See Section 4.2).

Name		Magnitude (S, J, E)			Modelled	Studied
Shapiro	shp	10 km	10 m	10 cm	S, J, E	J, E
Second Order	2nd	1 mm	10^{-8} m	10^{-12} m	S, J, E	S, J, E
J_2	J2	0.1 mm	1 cm	10^{-7} m	S, J, E	S, J, E
Velocity Light Time	vlt	1 mm	1 cm	1 cm	S, J, E	S, J, E

Table 3: Summary of relativistic light time effects considered in the experiment. Rough approximations for each effect are given for the Sun, Jupiter and Earth (S, J, E). When applicable, these values were checked against those given in [Hees et al., 2014, pp. 12,13]. "Modelled" effects are included in the truth model. Solar Shapiro is not studied, as the light-time calculator fails to converge when it is excluded from the estimation model (See Section 4.2).

4 Methodology

The impact on parameter estimates of each effect given in Section 3 was assessed using simulated experiments. The *TU Delft Astrodynamics Toolbox* (Tudat) software tool was used for these simulations. In this section we give a description of the experiment setup. The motivation for choosing Juno as our reference mission, as well as the exact orbit definition are covered in 4.1. An outline of the experiment setup is given in 4.2. Finally, the metrics used to express the experiment results are defined in Section 4.3.

4.1 Environment Definition

In our simulated experiments, we target a spacecraft in a Juno-like orbit around Jupiter. This choice is based on [Dirkx et al., 2018], which showed that ILR can potentially improve estimates of parameters whose influence on the observation signal had a long period (> 2 hours). Solar orbiters and spacecraft orbiting high above planets have especially long characteristic periods (days - years). Juno had a planned orbital period of 14 days, but ended up in a 54-day orbit due to a failed burn [Brown and Cantillo, 2017]. In addition to its long orbital period, Juno was used as a reference to verify our light time correction implementation against that of [Hees et al., 2014].

Our simulation environment includes the Sun, Earth and Jupiter, as well as our Juno-like spacecraft. Additionally, we place six laser ranging ground stations on Earth's surface. Two are placed on the poles, and four on the equator at longitudes of $0^\circ, 90^\circ, -90^\circ$ and 180° . This is done to ensure that the Earth does not occlude all ground stations from the spacecraft.

The Naif SPICE toolkit included in Tudat is used to approximate the state functions of the three celestial bodies [Acton, 2019]. An interpolated ephemeris based on tabulated planetary positions was used to define the orbits of the relevant celestial bodies. The spacecraft's state is propagated

numerically over a twelve-hour period around the periapsis. This part of the orbit is chosen because the proximity to Jupiter maximizes many of the light-time and acceleration effects being studied, meaning this interval has the largest potential to influence parameter estimates. The rest of the orbit is assumed to be roughly Keplerian. Propagation around the periapsis is repeated twelve times, with Jupiter having progressed in its orbit by 54 days each time. The first arc starts at midnight, 10 October 2016. Figure 2 shows a rough illustration of how the arcs are structured.

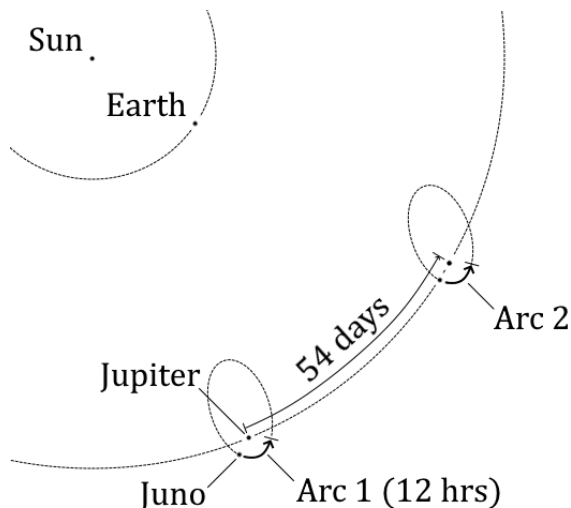


Figure 2: An illustration of the first two out of twelve propagation arcs (not to scale). The orientation of Juno’s orbit w.r.t. the inertial reference frame does not change between arcs, and the trajectory outside of the arcs is not propagated.

Quantity	Value	Quantity	Value
Periapsis radius	7.56×10^7 m	Observation interval	60 s
Apoapsis radius	8.10×10^9 m	Observation noise (σ)	1 mm
Inclination	89°	Number of arcs	12
Longitude of asc. node	30°	Arc duration	12 hrs
Argument of periapsis	10°		
μ of Jupiter	$1.26687 \times 10^{17} \text{ m}^3/\text{s}^2$		

Table 4: Definition of the spacecraft’s orbit at the beginning of an arc (left), and other values (right).

4.2 Experiment Overview

Our experiment is designed to study the impact of each relativistic effect in isolation. To achieve this, we run the parameter estimation process several times using different acceleration- and observation models. A nominal model (called the *truth model*) is defined, which includes all of the effects we are studying (See Section 3). For each run, a model used during parameter estimation (the *estimation model*) is defined which differs w.r.t. the truth model by exclusion of one relativistic effect.

The truth model is used to generate observations as an input to the parameter estimation process. These serve as a substitute for real ILR observations. After this, the estimation model is used in conjunction with this observation set to generate estimates for a given set of parameters. Specifically, we estimate the gravitational parameter μ of Jupiter, the post-Newtonian parameters γ and β , as well as the spacecraft’s state at the beginning of each arc. In addition to the parameter estimates

themselves, several other figures such as residuals and estimation errors are produced as outputs (See Section 4.3) Figure 3 illustrates how the truth- and estimation models are used during a given run of the experiment.

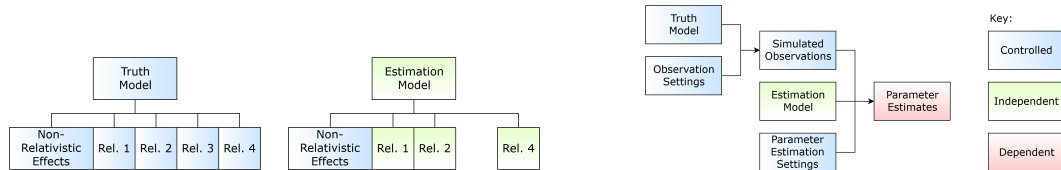


Figure 3: An illustration of the difference between the truth- and estimation models (left) and a top-level information flow diagram for a parameter estimation run (right). Here *independent* variables are intentionally varied between experiment runs to observe their effect on the *dependent* variables. *controlled* variables are kept the same between experiment runs.

The purpose of setting up the experiment in terms of a truth- and estimation model is to isolate modelling error as an independent variable. By making the exclusion of one relativistic modelling term the only explicit change between simulation runs, we can determine the relationship between individual effects and the resulting quality of parameter estimates. One basic hypothesis we can test is that the magnitude of parameter estimation error is proportional to that of the excluded effect. This requires the quantification of a modelling effect’s magnitude, which we can do through the preliminary estimates given in Section 3.4 and using the impact metrics described in Section 4.3.

In addition to the hypothesis described above, we will be able to determine the extent to which different model terms can compensate for one another. We can hypothesize that large effects such as the Newtonian point-mass gravity term, Schwarzschild acceleration and Shapiro light time effects of Jupiter could compensate for smaller accelerations and light time corrections that are excluded from the model. A similar approach (with a truth- and estimation model) was used in [Dirkx et al., 2016] to investigate the relationship between dynamical modelling and the properties of Jupiter’s moons.

Another approach to compensate for the absence of modelling terms is the estimation of empirical accelerations (“empiricals”). To investigate the influence of these, we run the entire experiment (one estimation run for each relativistic effect) twice. In one of these instances we include the estimation of empirical accelerations in the parameter vector, in addition to the spacecraft initial state, mass of Jupiter, γ and β . Specifically, we estimate a constant 3D acceleration vector in the spacecraft’s radial-, cross-track- and along-track directions. We estimate a separate empirical acceleration vector for each arc, resulting in a total of $12 \times 3 = 36$ additional parameters. Adding these parameters should be able to compensate for the exclusion of effects that are largely independent of orbit geometry (i.e. effects that are largely constant throughout an arc).

For each parameter estimation run, the following steps are carried out:

1. Define the environment (Sun, Jupiter, Earth, Juno, ground stations)
2. Create acceleration models (truth- and estimation)
3. Compute starting time and initial spacecraft state for each arc
4. Create observation models (truth- and estimation)
5. Specify parameters to be estimated
6. Generate a set of noisy observations using the truth model

7. Estimate the specified parameters using the generated observations

The spacecraft is influenced gravitationally by Jupiter and the Sun. For simplicity, we neglect other perturbing sources of gravity (e.g. Jupiter’s moons, Saturn, Earth) in our model. Additionally, all classical perturbing accelerations (e.g. spherical harmonic gravity, atmospheric drag, radiation pressure) are neglected. The only accelerations included in our model are Newtonian point-mass gravity and the relativistic terms given in 3.2. This minimal approach is used to ensure that only the effects under study influence the results.

The parameter estimation process is carried out using the iterative least squares gradient descent method. In short, a vector of parameters \mathbf{x} is estimated by starting with an initial guess that is updated over a number of iterations to obtain an least-squares parameter vector \mathbf{x}_{lsq} . The estimation process takes an observation vector \mathbf{z} and corresponding observation model $h(\mathbf{x})$ (which is also dependent on the spacecraft dynamical model) as its inputs. In our case \mathbf{z} is a vector of range measurements. On each iteration, the parameter vector is updated according to the following mapping: [Montenbruck and Gill, 2005, p.262]

$$\mathbf{x}_{lsq} \rightarrow \mathbf{x}_{lsq} + \Delta\mathbf{x}_{lsq} \quad \text{where} \quad \Delta\mathbf{x}_{lsq} = (H^TWH)^{-1} (H^TW(\mathbf{z} - \mathbf{h}(\mathbf{x}_{lsq}))) \quad (25)$$

Here H is the *normal matrix*, defined as $H = \partial\mathbf{h}/\partial\mathbf{x}_{lsq}$ and obtained by numerically integrating the variational equations (See e.g. [Montenbruck and Gill, 2005, ch.7.2]). W is the weight matrix given by $W = \text{diag}(\sigma_1^{-2}, \sigma_2^{-2}, \dots, \sigma_n^{-2})$, where σ_k is the expected error of the k^{th} observation. In our case we simply have $\sigma_k = 1$ mm for all observations. A full description of the weighted least-squares parameter estimation process can be found in [Montenbruck and Gill, 2005, ch.8].

The spacecraft state and variational equations were computed numerically using a Cowell propagation scheme (i.e. using Cartesian state coordinates) and a Runge-Kutta seventh-order integrator with a constant 10 s step size. By testing different step sizes and integrator types, this setup was found to be a good compromise between computation speed and results quality, with the total positional error at the end of an arc not exceeding 0.1 mm.

4.3 Impact Metrics

To quantify the relationship between relativistic modelling and parameter estimation error we use three different metrics: true-to-formal error ratio, observation errors and estimation residuals. In this section we define each metric and discuss how they are related to the experimental variables. In Section 5 the results are presented, which are given in terms of these metrics.

4.3.1 True-to-Formal Error Ratio

The first metric, *true-to-formal* error ratio, is used as a way to numerically quantify modelling error. As discussed above and shown in Figure 3, the main independent variable of the experiment is the list of terms included in the estimation model. While the magnitude of each term can be roughly estimated (as we have done in Section 3.4), a more rigorous estimate can be obtained by looking directly at the influence on parameter estimates. Because we have full access to the underlying parameters used in the truth model, we can compare these to the corresponding estimated values to obtain a *true error* figure ϵ_T . For example, given a true value of the PPN parameter $\gamma_T = 1$ and an estimated value γ_E , the true error is given by $\epsilon_{\gamma,T} = |\gamma_T - \gamma_E|$.

In a perfect estimation process (using an error-free model, noise-free observations and perfect numerical integration) ϵ_T should be zero. Conversely, any deviation of ϵ_T from zero can be interpreted as a measure of the listed error factors. The noise of our generated observations is Gaussian with a standard deviation of 1 mm, and our integrator has an estimated maximum error less than 0.1 mm.

Given this, any true error value greater than that of the control experiment (where the true- and estimation models are equal) should serve as a quantitative measure of the impact a given modelling term has on parameter estimates.

To make the comparison of error terms w.r.t. different parameters easier, we normalize the true error with respect to *formal error* ϵ_F . As mentioned above, the parameter estimates are obtained through an iterative least-squares gradient descent process. On any given iteration, the parameter covariance matrix C can be computed through $C = (H^T W H)^{-1}$, where H and W are the normal- and weight matrices of that iteration, respectively (See Equation 25). The diagonal entries of C are the estimated variances σ_p^2 of parameters p , and the formal errors of are in turn defined as their square roots: $\epsilon_{F,p} = \sigma_p$. As such, formal error serves as an estimate of the standard deviation of parameter estimation error, assuming said error is a random variable. [Montenbruck and Gill, 2005, p.264]

The ratio of these two error figures is simply called the true-to-formal error ratio or TF-ratio, $\epsilon_{TF} = \epsilon_T / \epsilon_F$. While the true error ϵ_T is directly related to the modelling error, ϵ_F can (and does, in our case) have a relatively small value even when modelling error is large. This is because ϵ_F is closely related to random errors, whereas the removal of a modelling term results in systematic observation errors. The result of this is that ϵ_F remains largely constant across our experiments (< 1% difference between control and the largest effect, Jupiter Schwarzschild light time). As such, the TF-ratio serves as a good numerical measure of the impact that removing a given relativistic modelling effect has on the resulting parameter estimates.

It is important to note that the TF-ratio can only be computed in theoretical studies such as this one, where the underlying parameters of the truth model are known. In any real-life effort to estimate astronomical parameters, their true values are not known at any point. The two remaining metrics described below can be computed in real experiments.

4.3.2 Observation Error

The second metric we use to gauge the relativistic effects is *observation error* ΔR . The range observations \mathbf{R}_T used as inputs to the parameter estimation process are generated using the truth model (See Figure 3). Using the same settings, we can generate another set of observations \mathbf{R}_E using the estimation model. We can eliminate the influence of noise either by generating noise-free \mathbf{R}_T and \mathbf{R}_E separately, or by generating both with the same noise values and subtracting them from one another. Either way, we define the vector of noise-free observation errors as $\Delta \mathbf{R} = |\mathbf{R}_T - \mathbf{R}_E|$. We can condense this into a single figure by taking the average of $\Delta \mathbf{R}$, yielding the mean absolute noise-free observation error $\Delta \bar{R}$. Unless otherwise specified, shorthand terms like "mean observation error" are used to refer to $\Delta \bar{R}$.

The mean observation error serves as a straightforward indicator of a modelling effect's magnitude. In the case of light time effects, $\Delta \bar{R}$ simply gives the mean value of the expressions given in Section 3.3, computed at the specified observation times. For acceleration effects, $\Delta \bar{R}$ gives an aggregated measure of how far the satellite deviates from its nominal orbit (i.e. the trajectory given by the truth model). Note that $\Delta \bar{R}$ is independent of the estimation process, as all the data is generated before any parameter estimation is carried out. As such, $\Delta \bar{R}$ can be regarded as pre-estimation observation error, in contrast to the residuals which can be seen as post-estimation observation errors (See following section).

In contrast to the TF-ratio, mean observation error is computable in a real experiment setting given that the formulation of a given effect is known. For light time effects, the entries in $\Delta \mathbf{R}$ can be computed directly using the expressions given in Equations 20 to 23 (and any additional light time correction expressions, depending on the experiment). The observation error due to acceleration modelling error can also be computed, but requires the spacecraft's orbit to be numerically

propagated.

4.3.3 Estimation Residuals

Finally, we use the vector of *residuals* $\boldsymbol{\rho}$ as an impact metric. For a given iteration of the least-squares estimation process, the residuals are defined as $\boldsymbol{\rho} = \mathbf{z} - \mathbf{h}(\mathbf{x}_{\text{lsq}})$. Here \mathbf{z} is the vector of observations (in our case the ranges \mathbf{R}) and $\mathbf{h}(\mathbf{x}_{\text{lsq}})$ is the modelled set of observations based on the current parameter estimates \mathbf{x}_{lsq} . Similarly to the mean observation error $\Delta\bar{R}$, we can condense the residual vector into a single value by taking the mean of the absolute residuals $\bar{\rho}$. Note that in this study we use the noise-free residuals, which we simply compute by subtracting the generated noise from the computed residuals. Because noise values cannot be reliably obtained from real observation data, any real experiment aiming to replicate our method will have to use noisy residuals.

As mentioned above, residuals $\boldsymbol{\rho}$ can be interpreted as the post-estimation equivalent of the observation error $\Delta\mathbf{R}$. Both can be computed in a real experimental setting, and as such the relationships and conclusions presented in the following sections could be applicable to such studies.

5 Results

In this section we present the results generated using the method described above. The three metrics introduced in Section 4.3 are used to gauge the impact of each relativistic effect on parameter estimates. Furthermore, two separate experiments were run where the estimation of empirical accelerations was included and excluded. In both cases we only look at the impact this on the four main parameters (state, μ_J , γ , β) and not the acceleration estimates themselves. We use the shorthand described in Section 3.4 to refer to relativistic effects. That is, [B,abr] refers to the effect pertaining to body B with the corresponding abbreviation "abr". Table 5 gives all of the abbreviations and body names used.

Effect Name	Abbreviation	Effect Name	Abbreviation
Point Mass Gravity	pmg	Shapiro	shp
Schwarzschild	sch	Second Order	2nd
Kinetic	kin	J_2	J2
External Potential	ext	Velocity Light Time	vlt
Central Body Velocity	cbv	Body Name	Abbreviation
Angular Momentum	ang	Sun	S
Extrinsic Gravitomagnetic	xgm	Jupiter	J
		Earth	E

Table 5: Summary of abbreviations used. Acceleration effects (Left), Light time effects (Right top) and celestial bodies (Right bottom).

We first give the true-to-formal error ratio values in Section 5.1 and compare these to our preliminary estimates. In Section 5.2 we compare the TF ratio values to the mean observation error, a more robust version of our preliminary estimates. Finally, in Section 5.3 we look at the influence that the estimation process has by comparing the pre- and post-estimation observation errors in the form of residuals. While there is some discussion in this section, the implications of the results will be discussed further in Section 6.

5.1 True-to-Formal Error Ratios

As discussed in Section 4.3.1, the true-to-formal error ratio ("TF ratio") is a dimensionless figure that is directly indicative of the impact modelling error has on the resulting parameter estimates.

In Figures 4 and 5 the TF ratios obtained from our simulations are presented directly. The two figures differ in whether empirical accelerations were estimated or not. For Figure 4 empiricals were not estimated, and for Figure 5 they were. Each experiment also includes a control run where the truth- and estimation models are the same (i.e. no effects are excluded).

Out of the 22 studied effects listed in Tables 2 and 3, 14 are displayed here. The eight remaining effects (namely [S,kin], [S,cbv], [S,ang], [S,xgm], [S,J2], [J,2nd], [E,2nd] and [E,J2]) were filtered out based on their negligible impact on observation error. Specifically, their mean absolute observation error $\Delta\bar{R}$ (See Section 4.3.2) was below a threshold of 10^{-5} m. In addition, their TF error ratios were close (within 1%) of TF ratio obtained from the control experiment.

There are some things we can note based on this initial set of filtered effects. For the Sun, only the largest dynamical effect, the Schwarzschild acceleration, has a significant impact on estimation error. Overall, the spacecraft’s distance from the Sun is too large for the remaining dynamical effects to be significant. Additionally, [S,kin], [S,cbv] and [S,xgm] depend on the Sun’s barycentric velocity, which is quite slow (around 20 m/s). Conversely, the Sun is the only body for which the second-order light time effect [S,2nd] is significant. The same is true for Jupiter and the J_2 light time effect. Looking at the preliminary estimates given in Table 3 we see a good agreement with the experimental results. All of the effects with an estimated magnitude of 0.1 mm or lower were found to have a negligible impact on estimation results, and vice versa.

We can compare the preliminary effect magnitude estimates made in Section 3.4 with the resulting parameter error. To recap, Table 2 gives conservative (i.e. large) estimates for the relative magnitudes of Jupiter’s acceleration effects. The Schwarzschild term is largest, at around 10^{-5} times the point mass gravity term. This is followed by [J,ang] and [J,xgm] at around 10^{-8} times the point mass term, and [J,kin], [J,ext] and [J,cbv] at 10^{-9} times. Comparing these values to the TF ratios, the order of the terms matches for the most part. Excluding [J,shp] from the dynamical has the greatest influence on TF ratio of the Jupiter acceleration terms, in all cases. This is followed by [J,ang] and [J,xgm], which again matches the preliminary estimates. While the remaining three effects also match the relative order of the estimates, [J,kin] and [J,ext] notably have much lower TF ratios than [J,cbv] for the state, γ and β parameters when no empiricals are estimated. This discrepancy is discussed further below, and in Section 6.

We can make similar comparisons between the preliminary estimates and TF ratios for the light time effects. With reference to Table 3, the largest effect is Jupiter’s Shapiro light time correction [J,shp] at around 10 m. This is followed by [E,shp] at around 10 cm. [J,J2], [J,vlt] and [E,vlt] all have magnitudes around 1 cm, and [S,2nd] and [S,vlt] both around 1 mm. Comparing these with Figures 4 and 5, we see that the order of the TF ratios generally matches the predictions. The main exception is [J,vlt], which has a slightly larger TF ratio than [E,shp]. This could be attributed to a poor initial estimate or something else. To determine the cause, we should look at more precise estimates of the

5.2 Comparison with Mean Observation Error

To make the comparison between true-to-formal error ratio and the magnitude of each effect more concrete, we can directly compute the average observation error $\Delta\bar{R}$ caused by removing each relativistic effect (See Section 4.3.2). For each experiment, two sets of noise-free observations were generated using the truth- and estimation models, respectively. By computing the absolute difference of these two observation sets and then taking the mean, we get a single figure called the mean absolute observation error $\Delta\bar{R}$. This metric is a more robust variant of the estimates computed in Section 3.4.

Figures 6 and 7 show plots of the TF ratio against $\Delta\bar{R}$ for the experiments excluding and including empirical acceleration estimates, respectively. We can see that the two metrics are correlated to

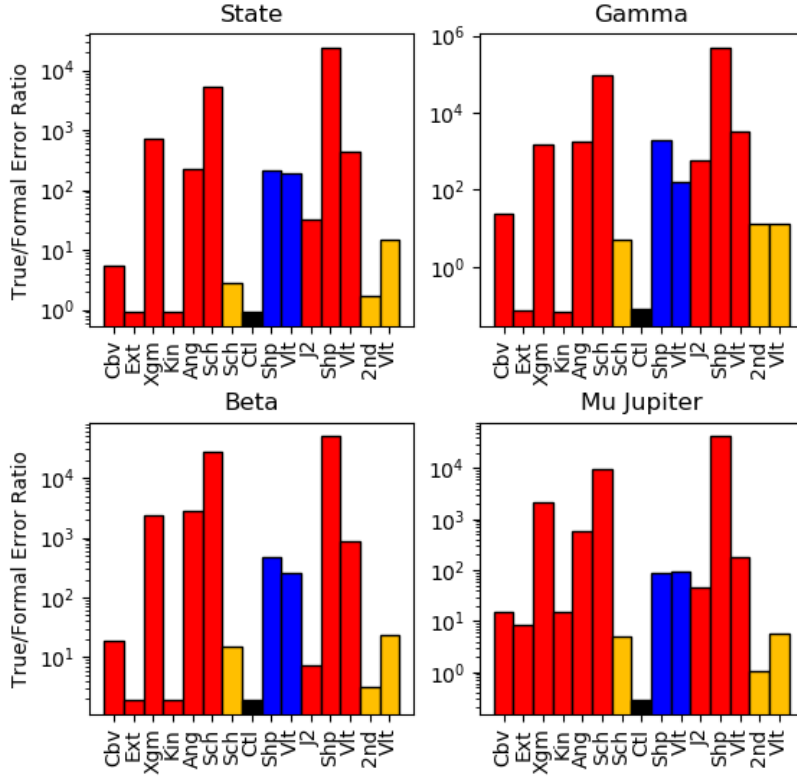


Figure 4: True-to-formal error ratio obtained when excluding the given effect from the estimation model. Red, yellow and blue bars represent Jupiter, the Sun and Earth, respectively. "Ctl" is the control experiment where the estimation- and truth models were the same.

some degree, with a large $\Delta\bar{R}$ being indicative of a large TF error ratio. This is to be expected, as both metrics are directly dependent on modelling error.

Performing an exponential fit (that is, a linear fit on the logarithmic data in given Figures 6 and 7) allows us to quantify the degree of correlation between $\Delta\bar{R}$ and ϵ_{TF} through the resulting R -value. Using all of the available data points, the correlation without empirical accelerations is fairly weak (between 0.4 and 0.8). However, if we ignore the two outliers [J,kin] and [J,ext], the correlation of the remaining points is fairly good (0.87 to 0.95).

Carrying out a similar process for the empirical acceleration experiment, the improvement is less pronounced. The degree of correlation improves somewhat from $R \approx 7.5$ to $R \approx 0.85$. Looking at the distribution of the data points, we see that there are many more but less extreme deviations from the best-fit line.

Overall, we observe that $\Delta\bar{R}$ and ϵ_{TF} become slightly less correlated when the estimation of empirical accelerations is introduced. However, the influence of the extreme outliers [J,kin] and [J,ext] is also reduced significantly. Looking the set of outliers that appear when estimating empiricals, we can see that they are largely acceleration effects, all having significantly lower TF ratios than should be expected based solely on the mean observation error. This result is to be expected, as the addition of

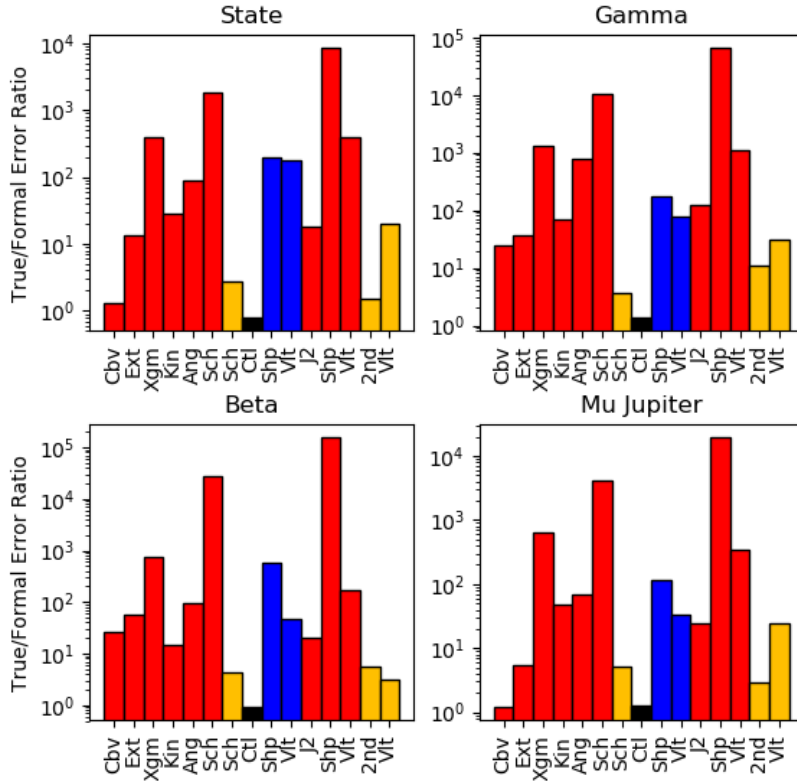


Figure 5: True-to-formal error ratio obtained when estimating empirical accelerations. Red, yellow and blue bars represent Jupiter, the Sun and Earth, respectively. "Ctl" is the control experiment where the estimation- and truth models were the same.

a constant empirical acceleration during each arc should be able to compensate for the exclusion of a relativistic acceleration modelling effect. While none of the dynamical effects studied are strictly constant throughout any given arc, empirical accelerations should still be able to compensate for some of the error, which is indeed what we observe.

5.3 Observation Errors and Residuals

The final impact metric we consider is the estimation residuals $\boldsymbol{\rho}$. As mentioned in Section 4.3.3, residuals are defined as the difference between real observations \mathbf{z} and modelled observations $\mathbf{h}(\mathbf{x}_{\text{lsq}})$ based on the current parameter estimates. Just like with the observation error $\Delta\mathbf{R}$, we can condense the residuals into a single figure by taking the mean of the absolute residuals, yielding the *mean absolute residual* $\bar{\rho}$. Note that we use the noise-free residuals, which is not possible in a real-life situation.

Because $\Delta\bar{R}$ and $\bar{\rho}$ can both be interpreted as an "observation error" measure, it makes sense to directly compare the two. Figure 8 plots $\bar{\rho}$ and $\Delta\bar{R}$ against one another, both with and without estimating empirical accelerations.

A notable feature of Figure 8 is that the mean residuals are always lower than the mean observation

Comparison of Observation Differences Between Truth- and Estimation Models

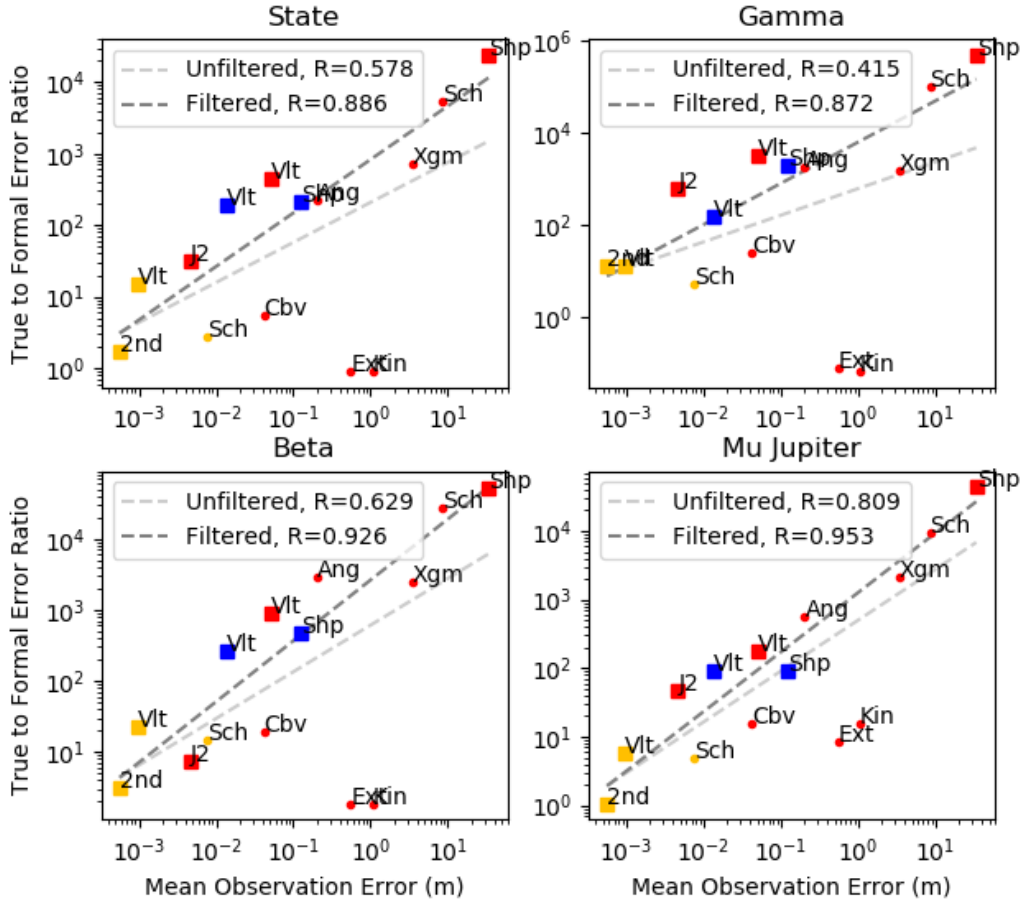


Figure 6: Comparison between the mean absolute observation error and true-to-formal error ratio when empirical accelerations were *not* estimated. Red, yellow and blue data points represent Jupiter, the Sun and Earth, respectively. The "Filtered" best fit line excludes the outliers [J,kin] and [J,ext].

errors. This is to be expected, as the estimation process aims to minimize the least-squares magnitude of the residual vector. As such it makes sense that $\bar{\rho} \leq \Delta \bar{R}$ in all of our experiments.

Comparing the two graphs, we can see that the residuals and observation errors are much closer to being equal when empirical accelerations are included in the estimation process. While one might conclude that lower residuals imply a more successful estimation process (i.e. more accurate parameter estimates), it is more likely that these small residual values are achieved by introducing error somewhere else. We have already seen in the previous section that including empirical accelerations generally results in better parameter estimates (i.e. lower TF ratios). In other words, the relatively low mean residual figures obtained come at the cost of poor parameter estimates.

Finally, looking at the graph where empirical accelerations are estimated (i.e. Figure 8 (Right)), we can easily identify a set of five outliers. These are [J,kin] and [J,ext], which we have identified previously, in addition to [J,xgm], [J,cbv] and [S,sch]. These are distinguished from the remaining effects in that they show a visible deviation from the nominal $\Delta \bar{R} = \bar{\rho}$ line. While it is not as clearly

Comparison of Observation Differences Between Truth- and Estimation Models

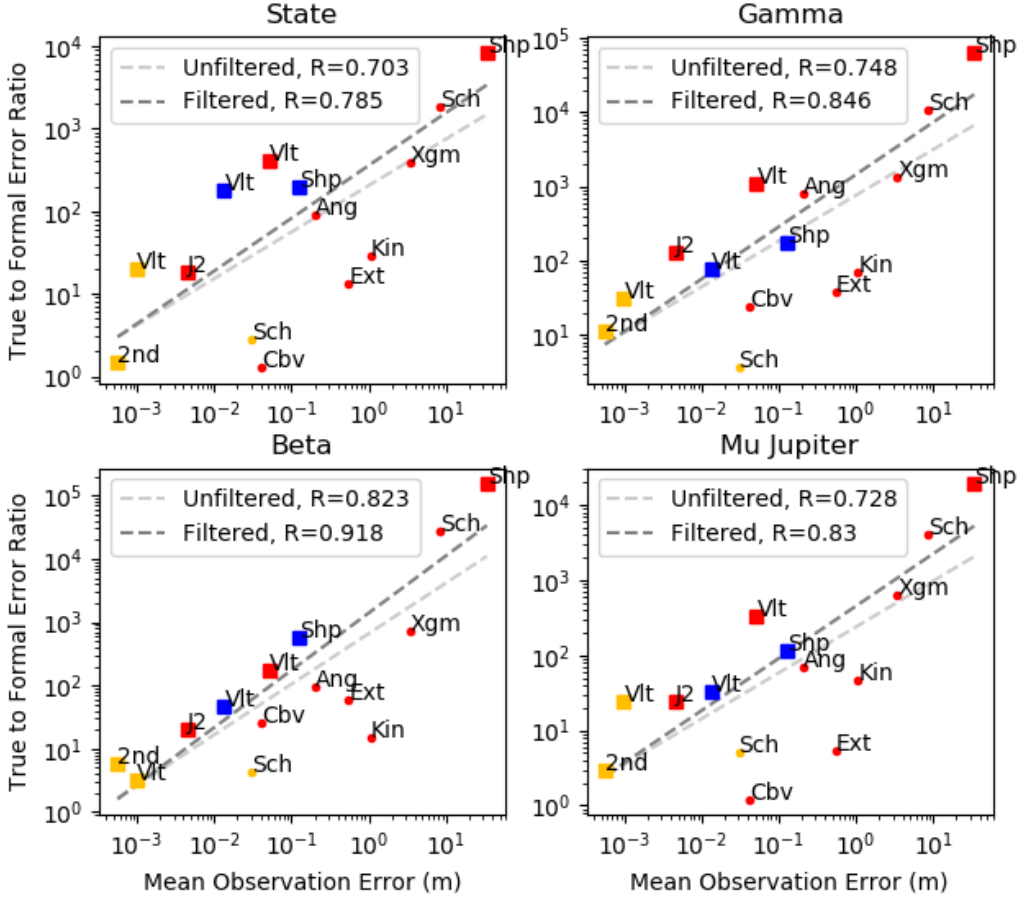


Figure 7: Comparison between the mean absolute observation error and true-to-formal error ratio when empirical accelerations were estimated. Red, yellow and blue data points represent Jupiter, the Sun and Earth, respectively. The "Filtered" best fit line excludes the outliers [J,kin] and [J,ext].

distinguishable in the empirical-free experiment, we can still see that the same five effects have very low mean residual figures compared to mean observation error. The mechanism by which these outliers manifest is likely through compensation in the model by a larger effect. For example, the kinetic acceleration term [J,kin] is proportional to the point-mass gravity term [J,pmg], assuming that the orbital speed of Jupiter is constant (See Equation 14). Because of this, excluding [J,kin] from the model results in the parameter estimates (likely μ_J in this case) being updated so that the the point-mass gravity term in the model effectively includes the contribution of [J,kin]. We discuss this mechanism in more detail in Section 6.2.

6 Discussion

Having presented the results of our simulations above, we now look at some of the key observations and their implications to potential real-life ILR campaigns. We first go over the usefulness of rough

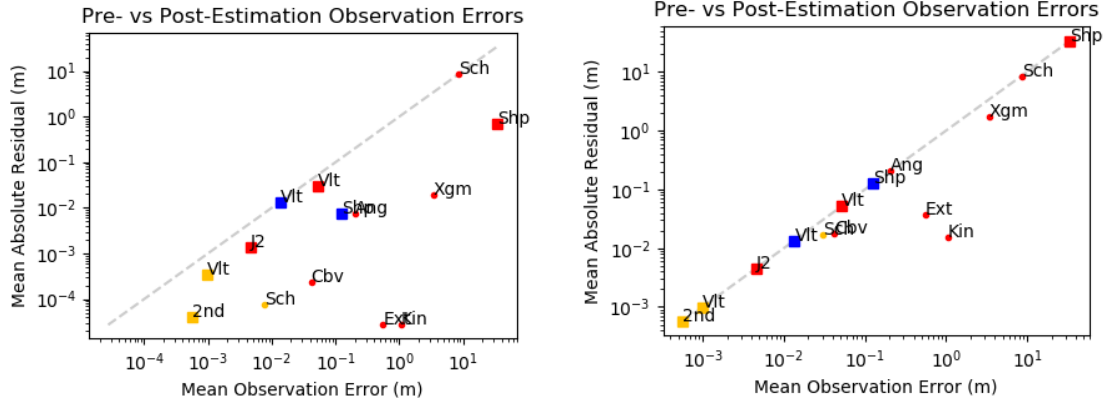


Figure 8: Comparison between mean absolute observation error and residuals, without (Left) and with (Right) the estimation of empirical accelerations. The diagonal line represents $\hat{\rho} = \Delta\bar{R}$.

preliminary estimates in Section 6.1. Then, in Section 6.2 we go over possible mechanisms by which different modelling effects can compensate for one another. Section 6.3 covers a similar discussion as it relates to empirical accelerations. Finally, in Section 6.4 we discuss what our observations mean from a broader perspective and look at possible ways by which the methods used here can be carried over and applied to real-life experiments involving ILR.

6.1 Utility of Preliminary Estimates

As was discussed briefly in Section 5.1, the preliminary estimates computed in Section 3.4 show some agreement with the numerical true-to-formal error ratio figures obtained through simulation. We can make the following observations about these preliminary estimates as they relate to the results:

- Effects with a negligible mean observation error $\Delta\bar{R}$ also showed a negligible deviation in true-to-formal error ratio with respect to the control experiment
- Light time effects that had a negligible influence on the results all had a preliminary estimated magnitude below the our observation noise level (i.e. 1 mm).
- Acceleration effects pertaining to Jupiter showed a general agreement in the relative magnitudes (i.e. their order from large to small) of the preliminary estimates and the TF error ratios. There are some exceptions, which are discussed in Sections 6.2 and 6.3.

While these rough preliminary estimates are not ideal data points and certainly should not be used as a substitute for simulation data, they do have the potential for some utility in a real parameter estimation effort. The main advantage is the ease with which these estimates can be computed from a given mathematical model. Because we observe at least some correspondence between the estimates and the final numerical results, they can be used as an initial step in filtering out negligible modelling terms. In our study, we retroactively filtered out eight relativistic effects based on the detailed simulation results. In a study where running a single parameter estimation run is more computationally expensive, this filtering step can be carried out in advance.

In addition to the above considerations, it should be noted that the mean observation error $\Delta\bar{R}$ is a potentially useful tool for filtering out negligible model terms as well. The preliminary estimates discussed so far are essentially a rough estimation of $\Delta\bar{R}$. Also, as mentioned in Section 4.3.2, mean observation error can be computed independent of the parameter estimation process. While it does

require fully setting up a numerical simulation, this can still be a desirable option is said simulation is significantly less computationally expensive than the estimation process. Based on Figures 6 and 7 we can observe that $\Delta\bar{R}$ and the TF ratio are fairly well correlated, with [J,kin] and [J,ext] being the main exceptions. As such, mean observation error could be used in place of (or in addition to) rough estimates as a tool to filter out negligible modelling effects.

In summary, the results obtained in this study serve as numerical verification that rough preliminary estimates of an effect's magnitude can be used with to narrow down the list of modelling terms that need to be taken into account during parameter estimation. These estimates can either be computed using the methods described in Section 3.4 or by running a preliminary simulation to obtain the mean absolute observation error $\Delta\bar{R}$. Other methods with a level of detail between these two approaches can of course also be devised.

6.2 Compensation by Larger Effects

Throughout Section 5 we made note of some outliers to the observed relationships and patterns. Specifically, exclusion of the kinetic gravity term of Jupiter [J,kin] and its external potential gravity [J,ext] from the dynamical model produced unexpected results. The true-to-formal error ratios and mean residual figures obtained from these two experiments were much lower than would be expected based on the pre-estimation observation error $\Delta\bar{R}$. Note that the former two metrics (TF ratio and $\bar{\rho}$) are both dependent on the parameter estimation process, while the mean observation error is not (See Section 4.3). This implies that these abnormal results are produced by the estimation process. Also, because the only variable that changes between experiment runs is the content of the estimation model, we can assume that the observed discrepancy are related to some form of modelling error. In this section we discuss a possible explanation for this phenomenon.

Let us first consider the parameter estimation run in which the kinetic acceleration due to Jupiter [J,kin] is excluded from the dynamical model. We end up with two models for the spacecraft's acceleration, $\mathbf{a}_{\text{truth}}$ and \mathbf{a}_{est} . The latter is missing one acceleration term with respect to the former, namely $\mathbf{a}_{\text{J,kin}}$. Recall that this term is given by $2(v_J/c)^2\mathbf{a}_{\text{J,pmg}}$, where v_J is the orbital speed of Jupiter and $\mathbf{a}_{\text{J,pmg}} = -(\mu_J/r_J^3)\mathbf{r}_J$. We can then express the two acceleration models explicitly as:

$$\begin{aligned} \mathbf{a}_{\text{truth}} = \mathbf{a}_{\text{J,pmg}} + \mathbf{a}_{\text{J,kin}} + \mathbf{a}_{\text{rest}} &= - \left(1 + 2 \frac{v_J^2}{c^2} \right) \frac{\mu_J}{r_J^3} \mathbf{r}_J + \mathbf{a}_{\text{rest}} \\ \mathbf{a}_{\text{est}} = \mathbf{a}_{\text{J,pmg}} + \mathbf{a}_{\text{rest}} &= - \frac{\mu_J}{r_J^3} \mathbf{r}_J + \mathbf{a}_{\text{rest}} \end{aligned} \quad (26)$$

Here \mathbf{a}_{rest} represents the remaining 11 relativistic acceleration effects in the model (See Table 2 under the "Modelled" column). All of these are included in both models, as the exclusion of $\mathbf{a}_{\text{J,kin}}$ is the only difference between them.

Based on this representation of the two models, we can see how the estimation process could compensate for the absence of the kinetic gravity term in estimation model \mathbf{a}_{est} . Over successive iterations, the values of the four parameters being estimated (μ_J , γ , β and spacecraft initial state) get updated in order to minimize the least-squares value of the residual vector (See Section 4.2). Consider the case where Jupiter's gravitational parameter is estimated to have a value of $\mu'_J = \mu_J + \Delta\mu_J$. Here μ_J is the true value of the parameter and $\Delta\mu_J$ is the true estimation error. The model then gets updated to the following:

$$\mathbf{a}'_{\text{est}} = \mathbf{a}'_{\text{pmg}} + \mathbf{a}'_{\text{rest}} = - \frac{\mu_J + \Delta\mu_J}{r_J^3} \mathbf{r}_J + \mathbf{a}'_{\text{rest}} = - \left(1 + \frac{\Delta\mu_J}{\mu_J} \right) \frac{\mu_J}{r_J^3} \mathbf{r}_J + \mathbf{a}'_{\text{rest}} \quad (27)$$

Here \mathbf{a}' denotes the acceleration model yielded by using the estimated value μ'_J rather than the true value μ_J . Note that all of the terms in \mathbf{a}_{rest} are proportional to c^{-2} , i.e. significantly smaller than \mathbf{a}_{pmg} . For this reason, we can say that the change in \mathbf{a}_{rest} due to $\Delta\mu_J$ is much smaller than the corresponding change in \mathbf{a}_{pmg} . For the remaining discussion, we will assume that $\mathbf{a}'_{\text{rest}} = \mathbf{a}_{\text{rest}}$.

Notice that the updated estimation model \mathbf{a}'_{est} looks similar to the truth model given in Equation 26. The only differences are between \mathbf{a}_{rest} and $\mathbf{a}'_{\text{rest}}$ (which we have neglected), and that $\Delta\mu_J/\mu_J$ is in the place of $2v_J^2/c^2$. Given an appropriate value of $\Delta\mu_J$, the point-mass gravity term in the estimation model can fully compensate for the absence of the kinetic gravity term. This value can be computed directly by:

$$\frac{\Delta\mu_J}{\mu_J} = 2\frac{v_J^2}{c^2} \quad \rightarrow \quad \Delta\mu_J = 2\frac{v_J^2}{c^2}\mu_J \approx 4.16 \times 10^8 m^3/s^2 \quad (28)$$

Here we have used the values from Table 1, namely $v_J = 12 \text{ km/s}$, $c = 300 \text{ Mm/s}$ and $\mu_J = 1.3 \times 10^{17} m^3/s^2$. We can compare this to the true parameter error of μ_J produced in our numerical simulation pertaining to [J,kin], namely $\Delta\mu_J = 4.28 \times 10^8 m^3/s^2$. This matches the above prediction to within a 3% margin, suggesting that the hypothesized mechanism is correct. Possible sources for the 3% error include the low-precision values for v_J , c and μ_J used, errors in our assumption that $\mathbf{a}'_{\text{rest}} = \mathbf{a}_{\text{rest}}$, and in the assumption that v_J remains constant throughout the Jovian year.

We can carry out a similar process for the external potential gravity term [J,ext]. Recall that $\mathbf{a}_{\text{J,ext}} = -(\mu_S/r_{SJ}c^2)\mathbf{a}_{\text{pmg}}$, where $\mu_S \approx 1.3 \times 10^{20} m^3/s^2$ is the gravitational parameter of the Sun and $r_{SJ} = 7.8 \times 10^{11} m$ is the orbital radius of Jupiter (See Equation 15). Repeating the same steps as for [J,kin], we can estimate the error term $\Delta\mu_J$ as:

$$\frac{\Delta\mu_J}{\mu_J} = -\frac{\mu_S}{r_{SJ}c^2} \quad \rightarrow \quad \Delta\mu_J = -\frac{\mu_S\mu_J}{r_{SJ}c^2} \approx -2.41 \times 10^8 m^3/s^2 \quad (29)$$

The error value obtained from our simulations is $\Delta\mu_J = -2.37 \times 10^8 m^3/s^2$, which matches the above prediction to within 2%. Again, this suggests that our proposed mechanism is indeed what is happening during the estimation process.

In addition to the accurate predictions provided above, we can observe the compensation through μ_J directly from our results. Looking back at Figure 4, specifically at the data for [J,kin] and [J,ext], we see that the true-to-formal error ratios are close to the control values for the initial state, γ and β . For μ_J the TF ratio is much larger, indicating that it is the only parameter that is used to compensate for the exclusion of the given modelling terms.

In summary, we have shown that in the experiments where the kinetic- and external potential gravity terms were excluded from the estimation model, the unexpectedly small values of TF ratio and mean residuals can be explained as compensation from the Newtonian point-mass gravity term. Looking at Figure 8 (Left), there are a number of other effects for which the mean residual is smaller than the mean observation error. However, if we look at the true-to-formal error ratios in Figure 4, we see no other examples of effects that are compensated for by the adjustment of a single parameter, as we showed above with μ_J . This could imply that the other effects are compensated for by another effect through the combined change of multiple parameters.

Let us investigate the extrinsic gravitomagnetic acceleration term of Jupiter, [J,xgm], as an example. From Equation 19 we obtain the expression for this acceleration term:

$$\mathbf{a}_{\text{J,xgm}} = \frac{2\mu_J(\gamma + 1)}{r_J^3 c^2} ((\mathbf{v}_J \cdot \mathbf{v})\mathbf{r}_J - (\mathbf{r}_J \cdot \mathbf{v})\mathbf{v}_J) \quad (30)$$

Because we perform our parameter estimation close to periapsis, the trajectory \mathbf{v} of the spacecraft and the radial vector \mathbf{r}_J are roughly perpendicular. That is to say $\mathbf{r} \cdot \mathbf{v} \approx 0$, meaning we can simplify the above expression by looking at only the first term. This acceleration component points in the direction \mathbf{r}_J , i.e. from the spacecraft toward Jupiter. Recall that in our discussion above, the missing acceleration effects were compensated for by the point-mass gravity term, which is the largest acceleration contribution. We should expect a similar relationship for [J,xgm], as it would not make sense for a very small gravitational effect to be able to compensate for a larger one. Intuitively, a large acceleration term should only require a small parameter estimation change to have a large compensatory influence on the missing gravity term.

Keeping this in mind, there are two main candidates for acceleration effects that can compensate for the absence of $\mathbf{a}_{J,xgm}$. These are the point-mass gravity and Schwarzschild acceleration terms of Jupiter. Both of these gravitational effects have contributions pointing in the radial direction toward Jupiter, which is what we are looking for. The point-mass gravity term is given by $\mathbf{a}_{pmg} = -(\mu_J/r_J^3)\mathbf{r}_J$. The radial term in the Schwarzschild acceleration is given by (See Equation 13):

$$\mathbf{a}_{J,sch,rad} = \frac{\mu_J}{r_J^3 c^2} \left(2(\gamma + \beta) \frac{\mu_J}{r_J} - \gamma v^2 \right) \mathbf{r}_J \quad (31)$$

With these candidate compensatory effects, we can make a few observations. First, $\mathbf{a}_{J,pmg}$ maintains largely the same magnitude throughout the Jovian year, which is not the case for the factor $\mathbf{v}_J \cdot \mathbf{v}$ that appears in $\mathbf{a}_{J,xgm}$. We can say the same for the different terms in $\mathbf{a}_{J,sch,rad}$, with none of the terms explicitly varying over the course of a Jovian year. Considering this, it is likely that primarily the point-mass gravity term compensates for the absence of $\mathbf{a}_{J,xgm}$ when it is excluded from the model. This is because, as discussed above, the fact that $\mathbf{a}_{J,pmg}$ is the largest acceleration effect means that a small adjustment in parameter estimates can compensate for the missing effect to a large degree without affecting the remaining acceleration terms too much.

From the above discussion, we can conclude that different relativistic modelling terms are not generally able to compensate for one another when an effect is omitted. While there were some coincidental cases in which a large effect was able to compensate for another (specifically the point mass gravity for the kinetic- and external potential terms) this is not generally the case. This problem could come up in a real parameter estimation study where not all of the relevant modelling terms are known. Another possible approach to dealing with potentially unknown modelling effects is through the use of empirical accelerations. This topic will be discussed in the following section.

6.3 Empirical Accelerations

In addition to investigating how different modelling effects compensate for one another when they are removed, we can introduce empirical accelerations into our parameter vector to actively compensate for certain effects. In this section we look at how our results were affected by introducing empiricals and we discuss possible alternatives and/or extensions to our approach.

As was mentioned earlier, two separate instances of the simulated experiments were run. In the first of these, no empirical accelerations were estimated. Only the arc-wise initial states, gravitational parameter of Jupiter and PPN parameters γ and β were included in the parameter vector. In the second instance, a constant empirical acceleration vector was estimated for each simulation arc. These vectors have components in the spacecraft's along-track, cross-track and radial directions. The results of these simulations have been presented in Section 5.

Overall, the addition of empirical accelerations resulted in better parameter estimation quality when excluding relativistic acceleration effects. This is clearly illustrated in Figure 7, where mean observation error is compared with true-to-formal error ratio. For the simulations pertaining to most of the

relativistic acceleration effects (specifically [J,ext], [J,kin], [J,xgm], [J,cbv] and [S,sch]) the TF ratios lie significantly below the best-fit lines. TF ratio measures the impact that modelling error has on parameter estimation quality. This means that, for the specified relativistic effects, the inclusion of empirical accelerations has successfully compensated for the exclusion of the given modelling term. The same five effects were identified in Section 5.3, based on the data points in Figure 8 (Right) with a significantly lower mean residual value than mean observation error.

The reason why empirical accelerations can compensate for the exclusion of these dynamical terms is fairly straightforward. Let us look at the central body velocity term of Jupiter, [J,cbv], as an example. Referring to Equation 16, the central body velocity acceleration is given by:

$$\mathbf{a}_{J,cbv} = \frac{\mu_J}{r_J^3 c^2} \cdot \frac{\mathbf{v}_J \cdot \mathbf{r}_J}{2} \left(3 \frac{\mathbf{v}_J \cdot \mathbf{r}_J}{r_J^2} \mathbf{r}_J - 2 \mathbf{v}_J \right) \quad (32)$$

Recall that \mathbf{v}_J is Jupiter's orbital velocity vector, and \mathbf{r}_J is spacecraft's position w.r.t. Jupiter. The acceleration effect given here can be separated into two terms, one aligned with the radial vector \mathbf{r}_J and the other with the along-track direction \mathbf{v}_J . Note that the dot product $\mathbf{v}_J \cdot \mathbf{r}_J$ is not constant throughout an arc, which means the empiricals cannot perfectly compensate for the missing dynamical term. During the estimation process, the relevant empirical acceleration estimates are updated to roughly compensate for the excluded dynamical effect. Compared to the situation where no empiricals are estimated, we should expect the residuals to be slightly smaller, as the accelerations during each arc are closer to those in the truth model.

Considering the discussion in Section 6.2, it is natural to ask why the TF ratio- and residual results for [J,kin] and [J,ext] are not as good as in the case where empiricals were not included. To explain this, consider the estimation model given in Equation 26, but with an extra term for the empirical acceleration \mathbf{a}_{emp} . This is the estimation model used for the experiment where [J,kin] is excluded:

$$\mathbf{a}_{est} = \mathbf{a}_{J,png} + \mathbf{a}_{emp} + \mathbf{a}_{rest} = -\frac{\mu_J}{r_J^3} \mathbf{r}_J + \mathbf{a}_{emp} + \mathbf{a}_{rest} \quad (33)$$

We can assume that \mathbf{a}_{emp} will get a significant nonzero value during the first few iterations in order to try to compensate for the missing term $\mathbf{a}_{J,kin}$. If we now try to carry out the same process as in Section 6.2 by perturbing μ_J , we now get the following estimation model (cf. Equation 27):

$$\mathbf{a}'_{est} = \mathbf{a}'_{png} + \mathbf{a}_{emp} + \mathbf{a}'_{rest} = -\left(1 + \frac{\Delta\mu_J}{\mu_J}\right) \frac{\mu_J}{r_J^3} \mathbf{r}_J + \mathbf{a}_{emp} + \mathbf{a}'_{rest} \quad (34)$$

Using the assumption that $\mathbf{a}'_{rest} = \mathbf{a}_{rest}$, we can solve for the appropriate value of the perturbation $\Delta\mu_J$ by equating our estimation model to the truth model given in Equation 26:

$$\begin{aligned} \mathbf{a}'_{est} &= \mathbf{a}_{truth} \\ -\left(1 + \frac{\Delta\mu_J}{\mu_J}\right) \frac{\mu_J}{r_J^3} \mathbf{r}_J + \mathbf{a}_{emp} + \mathbf{a}'_{rest} &= -\left(1 + 2 \frac{v_J^2}{c^2}\right) \frac{\mu_J}{r_J^3} \mathbf{r}_J + \mathbf{a}_{rest} \\ -\frac{\Delta\mu_J}{\mu_J} \cdot \frac{\mu_J}{r_J^3} \mathbf{r}_J + \mathbf{a}_{emp} &= -2 \frac{v_J^2}{c^2} \cdot \frac{\mu_J}{r_J^3} \mathbf{r}_J \\ \mathbf{a}_{emp} &= \left(\frac{\Delta\mu_J}{\mu_J} - 2 \frac{v_J^2}{c^2}\right) \frac{\mu_J}{r_J^3} \mathbf{r}_J \end{aligned} \quad (35)$$

The above equation is only solvable when \mathbf{a}_{emp} is a scalar multiple of \mathbf{r}_J . Because the orientation of \mathbf{r}_J changes throughout a given arc while \mathbf{a}_{emp} remains constant, we cannot solve the system in general. The only case where the equation is always solvable is if $\mathbf{a}_{\text{emp}} = \mathbf{0}$, which is only generally the case when empiricals are not estimated. This is why we see worse estimation results for [J,kin] and [J,ext] when empirical accelerations are included.

Having said this, it is important to remember that ideal inter-effect compensation relationships like those seen with [J,kin], [J,ext] and [J,pmg] are not generally present for all effects (See Section 6.2 concluding remarks). Additionally, there are many ways in which the experiment setup could be changed to potentially improve estimation quality. If more than one set of empirical accelerations is estimated for each arc, they will be able to compensate for missing effects in a more versatile way. Another approach is to parametrically vary the empirical acceleration estimates over an arc according to e.g. a sinusoidal curve. Both of these options are available in *Tudat*, the software library used to design our simulations.

6.4 Extensions and Generalizations

In this final section we will take a broader look at the topics covered above, and discuss how our observations can be applied to potential real-life ILR campaigns and/or further research.

First, let us consider the purpose of the discussion on effect compensation introduced in Sections 6.2 and 6.3. We were able to identify several cases where another relativistic effect or the estimation of empiricals was able to compensate for the excluded model term. However, while the purpose of our study is to gauge the impact of relativistic modelling by systematically excluding terms, in any real parameter estimation effort, sufficiently large model terms would never be excluded on purpose (here "sufficiently large" mean large enough to impact estimation results).

There are still some cases in which significant model terms might end up getting excluded. First, there is the case where not all of the relevant model terms are known for whatever reason (e.g. they have not yet been derived, do not have a practical mathematical representation etc.). It is also possible for effects to be incorrectly filtered out because they were deemed negligible based on preliminary estimates (See Section 6.1). In both of these cases, the compensatory behaviour discussed above could serve to increase parameter estimation quality. Out of the two phenomena we covered, estimating empirical accelerations will likely be more effective in most situations. While there are some cases where effects with similar mathematical representations can compensate for one another extremely well (see the example involving [J,kin] covered in Section 6.2), the use of empiricals is more likely to work in a diverse set of cases.

One of the features that is common to both of the compensation types discussed so far is that they are facilitated by the estimated parameters. In the example where point-mass gravity compensates for the kinetic gravitational term, the substituted term was generated by a change in the estimate of μ_J . Similarly, when empirical accelerations compensate for an omitted term, they do so by changing the estimated value(s) of the empiricals. Considering this, one potential avenue for further research is to determine how the set of estimated parameter choices affects the quality of estimation results. For instance, the example involving the gravitational influence of central body gravity discussed above (See Equation 32), the set of results may change if the velocity of Jupiter \mathbf{v}_J were included as an estimated parameter. Similar studies could be carried out specifically to quantify the impact that changing the parameter set has on estimation results.

In our preliminary investigation of the available modelling terms (See Section 3.4), 22 relativistic effects pertaining to different bodies were identified for study. There are two potentially interesting approaches that could be taken with this list of effects. First, one could extend our analysis to an experiment where two or more effects are omitted from the model at a time. This may help in

identify which model terms compensate for one another, as the compensation would fail when both effects are omitted simultaneously.

The opposite approach would be to break the currently identified effects down further into individual terms. For example, the central body velocity gravitational term could be broken into two separate effects as follows:

$$\mathbf{a}_{cbv} = \frac{\mu_b}{r_b^3 c^2} \cdot \frac{\mathbf{v}_b \cdot \mathbf{r}_b}{2} \left(3 \frac{\mathbf{v}_b \cdot \mathbf{r}_b}{r_b^2} \mathbf{r}_b - 2 \mathbf{v}_b \right) \quad \rightarrow \quad \begin{aligned} \mathbf{a}_{cbv,1} &= \frac{3\mu_b(\mathbf{v}_b \cdot \mathbf{r}_b)^2}{2r_b^5 c^2} \mathbf{r}_b \\ \mathbf{a}_{cbv,2} &= -\frac{\mu_b(\mathbf{v}_b \cdot \mathbf{r}_b)}{r_b^3 c^2} \mathbf{v}_b \end{aligned} \quad (36)$$

This would allow for more granular control over which modelling terms are excluded. This could in turn be combined with the above suggestion of excluding multiple terms at once, to determine how different relativistic terms are related. Doing the same for the light time effects might also make it possible to draw more conclusions about them, as the specific discussion so far largely pertains to acceleration terms.

The simulation scenario can be changed in order to determine whether the observations we have discussed so far hold in a more general sense. For example, the methodology used in this study could be modified to investigate a Martian or Saturnian orbiter. This could give insight as to the role that the central body properties play in influencing parameter estimates. In the case of a Mars probe, the central body is much smaller (compared to Jupiter, in our case) and closer to the ground station. All of the light time effects we have studied are directly dependent on the distance R to the target.

Finally, our base model could be extended to include most of the non-relativistic terms that are usually considered. This might include e.g. aerodynamic drag, radiation pressure, spherical harmonic gravity etc. These modelling terms would appear as part of the geodesic equation (See Equation 7) as an additional term. [Dirkx et al., 2015]

7 Conclusions & Recommendations

In summary, our objective was to investigate the relationship between relativistic modelling and the quality of parameter estimates obtained from ILR observation data. To fulfil this goal, we ran a series of simulated parameter estimation experiments using dynamical- and observation models of various fidelity levels. The reference spacecraft was chosen to be a Jovian orbiter similar to Juno. In an environment containing the Sun, Earth and Jupiter, we identified a list of 22 relativistic light-time (observation) and acceleration (dynamics) effects to investigate. For each simulation there were two models: the truth- and estimation model. The truth model always included all 22 relativistic effects, while the estimation model excluded a single effect. The truth model was used to generate a set of ILR observations, characterized as such by being two-way range measurements with a Gaussian noise level of 1 mm. These observations were used as inputs to a parameter estimation process.

In order to quantify the desired variables (relativistic modelling error and parameter estimation quality) we used three metrics. The mean absolute observation error served as a pre-estimation measure of the magnitude of a given effect. Estimation residuals represent the difference between actual observations and those produced by the estimation model. Finally, the true-to-formal (TF) error ratio served as a direct measure of the influence that modelling error had on parameter estimation quality. These three figures of merit were computed for each relativistic effect, and compared in order to determine the relative impact of each modelling term.

By comparing the resulting TF error ratio figures to our preliminary estimates of the magnitude of each effect, a correspondence could clearly be seen. The effects with the largest predicted magnitude had the greatest impact on estimation results, and vice versa. The TF ratio and mean pre-estimation observation error were positively correlated with a confidence degree of around $R = 0.8$ after filtering out the largest outliers. In addition, we were able to confirm that the effects with a predicted influence on observation error of less than 0.1 mm only had a negligible impact on parameter estimation quality. Considering this, we can conclude that preliminary estimates of an effect’s magnitude and/or simulated average observation errors generated before estimation, can be used as an effective tool for filtering out which relativistic effects are too small to necessitate inclusion in the estimation model.

While the mean observation error metric was largely indicative of parameter estimation error, there were a few cases in which the estimation error was significantly smaller than predicted. In particular, the gravitational influence of Jupiter’s speed and the Jupiter-Sun coupled gravity effect were found to be fully compensated for by other terms when left out of the model. Similar phenomena, to a lesser degree, could be observed with some of the other modelling effects. By analysing the two most significant cases, it was found that this compensation behaviour is facilitated by the larger effects in the model. By changing the estimated parameter values included in these large terms, the resulting change in acceleration behaves as a substitute for the missing effect. Overall, this type of compensation has an adverse impact on parameter estimation error.

Another method that can be used to compensate for missing modelling effects is the estimation of empirical accelerations. By adding a constant empirical acceleration vector for each arc to the list of estimated parameters, we saw a general decrease in the resulting estimation error in experiments where small acceleration terms were omitted from the model. This approach to compensating for missing modelling effects is preferable to relying on different terms to compensate for one another. Because the empirical accelerations are separate from the other parameters being estimated, changing them does not increase the estimation error of the important parameters. Furthermore, the number and type of empirical accelerations estimated can be freely adjusted depending on the need. As such, the use of empirical accelerations to compensate for missing relativistic effects is recommended for use over the reliance on compensation between existing effects.

There are a number of extensions and generalizations that can be explored in order to verify the conclusions made by this research. A more detailed study could be carried out where non-relativistic modelling terms such as drag, radiation pressure and spherical harmonic gravity are included. Another possible generalization is the investigations of different spacecraft orbits around different planets, such as Mars or Saturn.

Finally, in order to make the connections between this research and ILR more concrete, we recommend an extension to our method that looks specifically at the influence of noise modelling on the results. In our experiment, observation noise was modelled as a Gaussian variable with 1 mm standard deviation. This model could be extended to include systematic errors and instabilities with random-walk type behaviour (See [Dirkx et al., 2018, §3.4]). Such a study could be useful in characterizing the potential issues inherent to ILR.

References

- [Acton, 2019] Acton, C. (2019). SPICE - an observation geometry system for space science missions. Web. <https://naif.jpl.nasa.gov/naif/index.html>.
- [Bauer, 2017] Bauer, S. (2017). Application of one-way laser ranging data to the lunar reconnaissance orbiter (LRO) for time transfer, clock characterization and orbit determination. PhD Thesis, Technische Universität Berlin.

- [Bauer et al., 2017] Bauer, S., Hussmann, H., Oberst, J., Dirkx, D., Mao, D., Neumann, G., Mazarico, E., Torrence, M. H., McGarry, J. F., Smith, D. E., and Zuber, M. T. (2017). Analysis of one-way laser ranging data to LRO, time transfer and clock characterization. *Icarus*, 283.
- [Bertotti et al., 2003] Bertotti, B., Iess, L., and Tortora, P. (2003). A test of general relativity using radio links with the cassini spacecraft. *Nature*, 425.
- [Blanchet et al., 2001] Blanchet, L., Salomon, C., Teyssandier, P., and Wolf, P. (2001). Relativistic theory for time and frequency transfer to order c^{-3} . *Astronomy and Astrophysics*, 370.
- [Brown and Cantillo, 2017] Brown, D. and Cantillo, L. (2017). Nasa’s juno mission to remain in current orbit at jupiter. Press release. <https://www.nasa.gov/press-release/nasa-s-juno-mission-to-remain-in-current-orbit-at-jupiter/>.
- [Degnan, 2002] Degnan, J. J. (2002). Asynchronous laser transponders for precise interplanetary ranging and time transfer. *Journal of Geodynamics*, 34.
- [Dirkx et al., 2016] Dirkx, D., Lainey, V., Gurvits, L. I., and Visser, P. N. A. M. (2016). Dynamical modelling of the galilean moons for the JUICE mission. *Planetary and Space Science*, 134.
- [Dirkx et al., 2015] Dirkx, D., Noomen, R., Visser, P. N. A. M., Gurvits, L., and Vermeersen, L. L. A. (2015). Simultaneous spacetime dynamics estimation from space mission tracking data. *Astronomy and Astrophysics*, 587.
- [Dirkx et al., 2018] Dirkx, D., Prochazka, I., Bauer, S., Visser, P., Noomen, R., Gurvits, L. I., and Vermeersen, B. (2018). Laser and radio tracking for planetary science missions - a comparison. *Journal of Geodesy*.
- [Dirkx and Vermeersen, 2012] Dirkx, D. and Vermeersen, L. L. A. (2012). Interplanetary laser ranging - an emerging technology for planetary science missions. *EPSC Abstracts*, 7.
- [Hartle, 2003] Hartle, J. B. (2003). *Gravity - An Introduction to Einstein’s General Relativity*. Addison-Wesley.
- [Hees et al., 2014] Hees, A., Bertone, S., and Poncin-Lafitte, C. L. (2014). Light propagation in the field of a moving axisymmetric body: theory and application to juno. *Physical Review D*, 90.
- [Kopeikin et al., 2011] Kopeikin, S., Efroimsky, M., and Kaplan, G. (2011). *Relativistic Celestial Mechanics of the Solar System*. Wiley-VCH.
- [Kopeikin, 2010] Kopeikin, S. M. (2010). The gravitomagnetic influence on earth-orbiting spacecrafts on the lunar orbit. *Astrophysics and Space Science Library*, 367.
- [le Poncin-Lafitte et al., 2004] le Poncin-Lafitte, C., Linet, B., and Teyssandier, P. (2004). World function and time transfer: general post-minkowskian expansions. *Classical and Quantum Gravity*, 21.
- [Lissauer and de Pater, 2017] Lissauer, J. J. and de Pater, I. (2017). *Fundamental Planetary Science - Physics, Chemistry and Habitability*. Cambridge University Press, 4 edition.
- [Misner et al., 1973] Misner, C. W., Thorne, K. S., and Wheeler, J. A. (1973). *Gravitation*. W. H. Freeman and Company.
- [Montenbruck and Gill, 2005] Montenbruck, O. and Gill, E. (2005). *Satellite Orbits - Models, Methods and Applications*. Springer.
- [Murphy, 2013] Murphy, T. W. (2013). Lunar laser ranging: the millimeter challenge. *Reports on Progress in Physics*, 76.

- [Neumann et al., 2006] Neumann, G. A., Cavanaugh, J. F., Coyle, D. B., McGarry, J., Smith, D. E., Sun, X., Torrence, M., Zagwodski, T. W., and Zuber, M. T. (2006). Laser ranging at interplanetary distances. Web, NASA CDDIS. <https://cddis.nasa.gov/lw15/docs/papers/Laser%20Ranging%20at%20Interplanetary%20Distances.pdf>.
- [Neumann et al., 2005] Neumann, G. A., Cavanaugh, J. F., McGarry, J., Smith, D. E., Sun, X., Zagwodski, T. W., and Zuber, M. T. (2005). Asynchronous laser transponder experiment in deep space using messenger’s mercury laser altimeter. Poster, American Geophysical Union Fall Meeting.
- [Ni, 1972] Ni, W.-T. (1972). Theoretical framework for testing relativistic gravity. iv. a compendium of metric theories of gravity and their post-newtonian limits. *The Astrophysical Journal*, 176.
- [Noda et al., 2017] Noda, H., Kunimori, H., Mizuno, T., Senshu, H., Ogawa, N., Takeuchi, H., Moore, C., Pollard, A., Yamaguchi, T., Namiki, N., Kase, T., Saki, T., and Tsuda, Y. (2017). Laser link experiment with the hayabusa2 laser altimeter for in-flight alignment and measurement. *Earth, Planets and Space*, 69.
- [Pearlman et al., 2002] Pearlman, M. R., Degnan, J. J., and Bosworth, J. M. (2002). The international laser ranging service. *Advances in Space Research*, 30.
- [Petit and Luzum, 2010] Petit, G. and Luzum, B. (2010). IERS conventions (2010). International Earth Rotation and Reference System Service.
- [Shapiro, 1964] Shapiro, I. I. (1964). Fourth test of general relativity. *Physical Review Letters*, 13.
- [Smith et al., 2006] Smith, D. E., Zuber, M. T., Sun, X., Neumann, G. A., Cavanaugh, J. F., McGarry, J. F., and Zagwodski, T. W. (2006). Two-way laser link over interplanetary distance. *Science*, 311.
- [Soffel et al., 2003] Soffel, M. et al. (2003). The IAU 2000 Resolutions for Astrometry, Celestial Mechanics and Metrology in the Relativistic Framework: Explanatory Supplement. *The Astrophysical Journal*, 126.
- [Synge, 1931] Synge, J. L. (1931). A characteristic function in riemannian space and its application to the solution of geodesic triangles. *Proceedings of the London Mathematical Society*, 32.
- [Teyssandier and le Poncin-Lafitte, 2008] Teyssandier, P. and le Poncin-Lafitte, C. (2008). General post-Minkowskian expansion of time transfer functions. *Classical and Quantum Gravity*, 25.
- [Turyshchev et al., 2010] Turyshchev, S. G., Farr, W., Folkner, W. M., Giererd, A. R., Hemmati, H., Jr., T. W. M., Williams, J. G., and Degnan, J. J. (2010). Advancing tests of relativistic gravity via laser ranging to phobos. *Experimental Astronomy*, 28.
- [Will, 1971] Will, C. M. (1971). Theoretical frameworks for testing relativistic gravity. ii. parametrized post-newtonian hydrodynamics, and the nordtvedt effect. *The Astrophysical Journal*, 163.

3

Conclusions & Recommendations

In this thesis we aimed to answer the following research question:

How do individual relativistic modelling effects impact the estimates of spacecraft ephemerides and environmental parameters obtained using ILR observation data?

To achieve this goal, we used a series of simulated parameter estimation experiments in which individual relativistic terms were selectively excluded from the estimation model. To incorporate ILR observations were modelled through a two-way range measurements with a noise level of 1 mm, based on estimates from [10]. We investigated 22 relativistic effects and gauged their impact using the metrics of true-to-formal (TF) error ratio, mean observation errors and mean residuals. Out of these, mean observation error is most directly indicative of modelling error. The other two figures, TF ratio and residuals, are indicative of parameter estimation quality. This allowed us to use these metrics as quantitative measures of the two factors mentioned in the research question: relativistic modelling error and ephemeride/parameter estimates.

Comparing mean observation error with our TF ratio results, we were able to establish that these two factors are correlated. It was also found that relativistic effects with negligible mean observation error (<0.01 mm) corresponded to a negligible deviation in TF ratio from the control experiment. The same relationship was observed with the preliminary estimates computed in Section 2.3.4. For real ILR studies, this relationship can be used as a relatively low-effort way of filtering out negligible modelling effects without extensive software implementation.

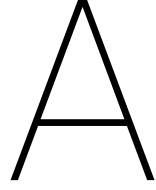
In addition to establishing the basic correlation between relativistic modelling error and parameter estimation quality, we looked at the major exceptions to the observed pattern. In particular, the exclusion of the kinetic- and external potential gravity terms of Jupiter from the estimation model was almost entirely compensated for by the much larger Newtonian point-mass gravity term. To summarize the discussion in Section 2.6.2, a small change in the estimated gravitational parameter of Jupiter changed the point-mass acceleration sufficiently to completely substitute the absent relativistic effect. This phenomenon is dependent on the fact that these relativistic accelerations and the point mass gravity term are proportional to one another. More generally, these compensatory relationships are dependent on the mathematical formulation of the underlying model term. Additionally, the fact that this compensation process is facilitated by modifying one of the parameter estimates makes it difficult and non-ideal to utilize this type of compensation in any real ILR study.

The inclusion of empirical accelerations in the estimation model is a much more practical way of compensating for missing relativistic effects. We re-ran our simulated experiments while estimating a constant empirical acceleration vector for each arc. In the corresponding results we saw a significant improvement in the TF ratio figures and mean residuals of most relativistic acceleration effects. Because empirical accelerations are a separate parameter that is independent of the physical and astronomical parameters like μ_J , this compensation process does not have as significant of an effect on parameter estimation error. We are also free to change the frequency and nature (e.g. constant vs. sinusoidal) by which empiricals are estimated, allowing a large amount of control over the degree to which they compensate for missing acceleration terms. We recommend

a further investigation of the relationship between different empirical acceleration setups and the resulting parameter estimation quality. Such an investigation could serve to provide real ILR studies with guidelines as to how frequently empirical accelerations should be estimated, and what the risks are of introducing too many acceleration estimates.

Furthermore, we recommend an extension to our research that explores different mission types in order to either support or contrast the results we obtained in our study of a highly elliptical Jovian orbiter. ILR missions targetting spacecraft in circular orbits, around other planets or in heliocentric orbit are possible mission types that could be investigated. This type of study could help inform various ILR studies about whether the results obtained here are more widely applicable or not.

Finally, we recommend that a more detailed study is carried out on the effects of observation noise modelling on e.g. parameter estimation quality. A comprehensive list of ILR noise sources and estimates was given in [10]. In our experiment we simplified these estimates down into a single Gaussian noise variable with a magnitude of 1 mm. A more detailed look at the influence of noise modelling on our results, including the systematic errors and "random walk"-type instabilities could help tie this research more closely to the inherent characteristics of ILR.



Acceleration Model Derivation

Out of the relativistic acceleration effects we studied, only the expressions for Schwarzschild- and Lense-Thirring acceleration were obtained from literature. The remaining effects were derived from the relativistic equations of motion and a post-Newtonian variant of the IAU 2000 spacetime metric [30]. In this appendix we present these derivations. We also re-derive the Schwarzschild metric to verify that our formulation of the equations of motion is accurate.

A.1. Relativistic Equations of Motion

By associating a body of interest with a set of events that coincide with e.g. its centre of mass, we can assign it with a four-dimensional position tensor $x^\mu(\tau)$ that describes its world line. This tensor and its derivatives are called its four-position, four-velocity and four-acceleration [11]. The relativistic motion of a body through spacetime can be fully described by the evolution of its four-position and four-velocity with respect to time. Just like in classical mechanics, position and velocity describe the state of a body. The derivative of these indicate how the state evolves over time. The only information that is required in addition to the state is the body's acceleration, i.e. the second derivative of x^μ w.r.t. proper time τ . This is given by the geodesic equation: [8] [16]

$$\frac{d^2 x^\mu}{d\tau^2} = -\Gamma_{\alpha\beta}^\mu \frac{dx^\alpha}{d\tau} \frac{dx^\beta}{d\tau} + A_{NC}^\mu \quad \text{where} \quad \Gamma_{\alpha\beta}^\mu = \frac{1}{2} g^{\mu\nu} \left(\frac{\partial h_{\nu\alpha}}{\partial x^\beta} + \frac{\partial h_{\nu\beta}}{\partial x^\alpha} - \frac{\partial h_{\alpha\beta}}{\partial x^\nu} \right) \quad (\text{A.1})$$

Here $\Gamma_{\alpha\beta}^\mu$ are the Christoffel symbols, which depend on the spacetime metric $g_{\mu\nu}$. $h_{\mu\nu} = g_{\mu\nu} - \eta_{\mu\nu}$ is the non-constant part of the metric. A_{NC}^μ non-conservative accelerations such as drag, radiation pressure and magnetic forces. In our analysis this term is neglected as we only model gravitational acceleration.

While Equation A.1 can be used to represent the dynamics of a relativistic object, it is more convenient to use an equivalent formulation in terms of the coordinate time t . Such a formulation is given by [16]. Because $d^2 x^0 / dt^2 = dc/dt = 0$, we only consider the spatial coordinates x^i :

$$\frac{d^2 x^i}{dt^2} = -c^2 \Gamma_{00}^i - 2c \Gamma_{0j}^i \frac{dx^j}{dt} - \Gamma_{jk}^i \frac{dx^j}{dt} \frac{dx^k}{dt} + \frac{dx^i}{dt} \left(c \Gamma_{00}^0 + 2 \Gamma_{0j}^0 \frac{dx^j}{dt} + \frac{1}{c} \Gamma_{jk}^0 \frac{dx^j}{dt} \frac{dx^k}{dt} \right) \quad (\text{A.2})$$

For the spacetime metric, we use the one given by the IAU 2000 relativistic framework resolutions [30], with the inclusion of post-Newtonian parameters γ and β : [8] [23] [35]

$$\begin{aligned}
h_{00} &= \frac{2w}{c^2} - \frac{2\beta w^2}{c^4} + \mathcal{O}(c^{-5}) \\
h_{0i} &= -(\gamma + 1) \frac{2w^i}{c^3} + \mathcal{O}(c^{-5}) \\
h_{ij} &= \delta_{ij} \frac{2\gamma w}{c^2} + \mathcal{O}(c^{-4})
\end{aligned} \tag{A.3}$$

Here w and w^i are called the relativistic scalar- and vector potentials, respectively. The Kronecker delta δ_{ij} has a value of 1 when $i = j$, and 0 otherwise.

In the same way that classical gravitational potential $U(t, \mathbf{r})$ relates the distribution of mass to the value of a gravitational field, the relativistic potentials w and w^i relate mass-, energy- and momentum distribution to spacetime curvature. The relationship between the stress-energy tensor $T_{\mu\nu}$ (See Equation 2.3) and relativistic potential is given by [30, p.2693].

The scalar potential can be expressed as the superposition of potentials caused by a set of bodies B , i.e. $w = \sum_{b \in B} w_b$. Each such potential can in turn be decomposed into the classical/Newtonian component w_0 and a relativistic correction term Δ : [8] [30, p.2698]

$$w_b = w_{0,b} - \Delta w_b / c^2 \quad \text{where} \quad \Delta w_b = \frac{GM_b}{r_b} \left(-2v_b^2 + \sum_{a \neq b} w_{0,a} + \frac{(\mathbf{v}_b \cdot \mathbf{r}_b)^2}{2r_b^2} + \frac{\mathbf{a}_b \cdot \mathbf{r}_b}{2} \right) \tag{A.4}$$

The vector potential can be split into an *intrinsic* term caused by the central body's rotation and an *extrinsic* part related to its linear motion [15]. These can be expressed as follows:

$$w_b^i = \frac{G(\mathbf{S}_b \times \mathbf{r}_b)^i}{2r_b^3} + w_{0,b} v_b^i \tag{A.5}$$

Here $r_b = |\mathbf{r}_b|$ is the position where the potential is calculated (e.g. the spacecraft position) measured with respect to b 's centre. $v_b = |\mathbf{v}_b|$ and \mathbf{a}_b are the velocity and acceleration of b in some inertial reference frame [8]. We later use \mathbf{v} and \mathbf{a} to denote the velocity and acceleration of the spacecraft (that is, $\dot{\mathbf{r}}_b = \mathbf{v}$, $\dot{\mathbf{v}} = \mathbf{a}$). The external potentials $w_{0,a}$ are the potential experienced at b 's centroid due to another body $a \in B$. \mathbf{S}_b is the central body's angular momentum vector.

The classical potential w_0 can be modelled in different ways, with the spherical harmonic expansion being a common approach: [14, p.406]

$$w_{0,b} = \frac{GM_b}{r_b} \left[1 + \sum_{n=2}^{\infty} \sum_{m=0}^n \left(\frac{R_{eq,b}}{r_b} \right)^n (C_{nm} \cos(m\lambda_b) + S_{nm} \sin(m\lambda_b)) P_{nm}(\sin(\phi_b)) \right] \tag{A.6}$$

In our case, we ignore all higher-order spherical harmonic terms for acceleration modelling. That is, we assume that $w_{0,b} = GM_b / r_b$. The justification for this is similar to our neglect of the non-conservative accelerations A_{NC}^μ . Because we are studying the effects of relativistic modelling, it is unnecessary to include accelerations in our model that we are not explicitly interested in. The contribution of $C_{20} = J_2$ is included in our model for the light time delay (See Section 2.3.3), as its magnitude is large enough ($\mathcal{O}(1 \text{ cm})$ for Jupiter) to be potentially significant.

Given our metric, we can further expand our equations of motion (Equation A.2) by evaluating the Christoffel symbols $\Gamma_{\alpha\beta}^\mu$. Using the metric in Equation 2.4, the expansions are given by [8] (which were based on [16, p.382]) in terms of partial derivatives of the relativistic potentials:

$$\begin{aligned}
\Gamma_{00}^0 &= \mathcal{O}(c^{-4}) \\
\Gamma_{0i}^0 &= -c^{-2}w_{,i} + \mathcal{O}(c^{-3}) \\
\Gamma_{00}^i &= -c^{-2}w_{,i} + 2c^{-4}(\gamma + \beta)w \cdot w_{,i} + \mathcal{O}(c^{-5}) \\
\Gamma_{0k}^i &= c^{-3}(\gamma + 1)(w_{,i}^k - w_{,k}^i) + \mathcal{O}(c^{-4}) \\
\Gamma_{ik}^0 &= c^{-3}(\gamma + 1)(w_{,k}^i + w_{,i}^k) + \mathcal{O}(c^{-4}) \\
\Gamma_{jk}^i &= c^{-2}\gamma(\delta_{ij}w_{,k} + \delta_{ik}w_{,j} - \delta_{jk}w_{,i}) + \mathcal{O}(c^{-3})
\end{aligned} \tag{A.7}$$

Here the subscript , i represent partial differentiation w.r.t. the spatial coordinate x^i . Because the potentials in Equations A.4 and A.5 do not depend explicitly on time, all time-derivative terms $w_{,t}$ have been omitted from the above expansions. Substituting these expanded Christoffel symbols into Equation A.2 yields the following:

$$\begin{aligned}
\ddot{x}^i &= w_{,i} + \frac{1}{c^2} \left[\dot{x}^j \dot{x}^k \gamma (\delta_{jk} w_{,i} - \delta_{ij} w_{,k} - \delta_{ik} w_{,j}) - 2(\gamma + \beta) w \cdot w_{,i} - \dots \right. \\
&\quad \left. \dots - 2\dot{x}^i \dot{x}^j w_{,j} + 2(\gamma + 1) \dot{x}^j (w_{,j}^i - w_{,i}^j) \right] + \mathcal{O}(c^{-3})
\end{aligned} \tag{A.8}$$

Here we have used the shorthand $\dot{x}^a = dx^a/dt$. We have also omitted terms proportional to c^{-4} , as these effects are too small to have a measurable impact on our results.

In the coming sections, we use the framework outlined above to derive various relativistic acceleration terms. For each effect, we take a term from the relativistic potentials (Equations A.4 and A.5) and substitute them into the equation of motion (Equation A.8). This results in a collection of relativistic effects that we can study individually, as presented in Section 2.4.

A.2. Schwarzschild Term

The Schwarzschild term can be derived using the Newtonian scalar potential $w_0 = \mu/r$ and computing its second-order contribution to the acceleration. Since the potential is not a function of t , the $w_{0,t}$ term can be ignored. That is:

$$\ddot{x}_{\text{sch}}^i = \frac{1}{c^2} \left[\dot{x}^j \dot{x}^k \gamma (\delta_{jk} w_{0,i} - \delta_{ij} w_{0,k} - \delta_{ik} w_{0,j}) - 2(\gamma + \beta) w_0 \cdot w_{0,i} - 2\dot{x}^i \dot{x}^j w_{0,j} \right] \tag{A.9}$$

Taking the spatial derivative of w_0 yields $w_{0,i} = -x^i \mu_b / r_b^3$. Substituting this into Equation A.9 yields:

$$\begin{aligned}
\ddot{x}_{\text{sch}}^i &= \frac{1}{c^2} \left[\gamma (\dot{x}^j)^2 w_{0,i} - 2\gamma \dot{x}^i \dot{x}^j w_{0,j} - 2(\gamma + \beta) w_0 \cdot w_{0,i} - 2\dot{x}^i \dot{x}^j w_{0,j} \right] \\
&= \frac{1}{c^2} \left[-\gamma (\dot{x}^j)^2 x^i \frac{\mu_b}{r_b^3} + 2(\gamma + \beta) x^i \frac{\mu_b}{r_b^3} \cdot \frac{\mu_b}{r_b} + 2(1 + \gamma) \dot{x}^i \dot{x}^j x^j \frac{\mu_b}{r_b^3} \right] \\
&= \frac{\mu_b}{r_b^3 c^2} \left[\left(2(\gamma + \beta) \frac{\mu_b}{r_b} - (\dot{x}^j)^2 \right) x^i + 2(1 + \gamma) (\dot{x}^j \dot{x}^j) \dot{x}^i \right]
\end{aligned} \tag{A.10}$$

Finally, we switch from tensor- to vector notation. First, all occurrences of x^i and its derivatives can be replaced with \mathbf{r}_b , \mathbf{v} and \mathbf{a} . Note that \mathbf{v}_b and \mathbf{a}_b are used to represent the barycentric motion of the central body (See Sections A.3, A.5, A.6 and A.8). We can also iterate over the index j and make the substitutions $(x^j)^2 = v^2$ and $\dot{x}^j \dot{x}^j = \mathbf{r}_b \cdot \mathbf{v}$. This produces the following expression for the Schwarzschild acceleration:

$$\mathbf{a}_{\text{sch}} = \frac{\mu_b}{r_b^3 c^2} \left[\left(2(\gamma + \beta) \frac{\mu_b}{r_b} - \gamma v^2 \right) \mathbf{r}_b + 2(1 + \gamma) (\mathbf{r}_b \cdot \mathbf{v}) \mathbf{v} \right] \tag{A.11}$$

This matches the expression for the Schwarzschild term given in [26, p.155].

A.3. Kinetic Term

The kinetic acceleration term produced by the squared speed of the central body v_b^2 , hence the name. We can isolate this part of the scalar potential, referring to Equation 2.5:

$$w_{\text{kin}} = \frac{2\mu_b}{r_b} \cdot \frac{v_b^2}{c^2} \quad (\text{A.12})$$

We then compute the first-order term of Equation A.8 using this part of the potential. That is:

$$\ddot{x}_{\text{kin}}^i = w_{\text{kin},i} = \frac{2\mu}{c^2} v_b^2 \cdot \frac{\partial}{\partial x^i} \frac{1}{r_b} = -\frac{2\mu v_b^2}{r_b^3 c^2} x^i \quad (\text{A.13})$$

And finally, converting to vector form:

$$\mathbf{a}_{\text{kin}} = -\frac{2\mu_b v_b^2}{r_b^3 c^2} \mathbf{r}_b \quad (\text{A.14})$$

A.4. External Potential Term

Just like the kinetic term, the acceleration due to external potentials is computed by isolating the second term in Δw_b . For simplicity, we consider the influence of a single body a :

$$w_{\text{ext}} = -\frac{\mu_b}{r_b c^2} w_{0,a} = -\frac{\mu_b \mu_a}{r_b c^2 r_{ab}} \quad (\text{A.15})$$

Here r_{ab} is the distance between a and b , which is independent of x^i and hence a constant under partial differentiation. Substituting w_{ext} into the first-order acceleration term:

$$\ddot{x}_{\text{ext}}^i = -\frac{\mu_b \mu_a}{c^2 r_{ab}} \cdot \frac{\partial}{\partial x^i} \frac{1}{r} = \frac{\mu_b \mu_a}{r_b^3 c^2 r_{ab}} x^i \quad (\text{A.16})$$

Converting this to vector form, we get:

$$\mathbf{a}_{\text{ext}} = \frac{\mu_b \mu_a}{r_b^3 c^2 r_{ab}} \mathbf{r}_b \quad (\text{A.17})$$

A.5. Central Body Velocity Term

The next term is derived from the third term in Δw_b , namely:

$$w_{\text{cbv}} = -\frac{\mu_b}{2c^2} \cdot \frac{(\mathbf{v}_b \cdot \mathbf{r}_b)^2}{r_b^3} \quad (\text{A.18})$$

Here both the numerator and denominator are dependent on x^i , yielding the following partial differentiation result:

$$\begin{aligned} \ddot{x}_{\text{cbv}}^i &= -\frac{\mu_b}{2c^2} \cdot \left[\left(\frac{\partial}{\partial x^i} (\mathbf{v}_b \cdot \mathbf{r}_b)^2 \right) \cdot \frac{1}{r_b^3} + \left(\frac{\partial}{\partial x^i} \frac{1}{r_b^3} \right) \cdot (\mathbf{v}_b \cdot \mathbf{r}_b)^2 \right] \\ &= -\frac{\mu_b}{2c^2} \left[\left(2v_b^i \cdot (\mathbf{v}_b \cdot \mathbf{r}_b) \right) \cdot \frac{1}{r_b^3} + \left(-3x^i \cdot \frac{1}{r_b^5} \right) \cdot (\mathbf{v}_b \cdot \mathbf{r}_b)^2 \right] \\ &= \frac{\mu_b}{r_b^3 c^2} \cdot \frac{\mathbf{v}_b \cdot \mathbf{r}_b}{2} \left[3 \frac{\mathbf{v}_b \cdot \mathbf{r}_b}{r_b^2} x^i - 2v_b^i \right] \end{aligned} \quad (\text{A.19})$$

Finally, switching to vector notation we get:

$$\mathbf{a}_{cbv} = \frac{\mu_b}{r_b^3 c^2} \cdot \frac{\mathbf{v}_b \cdot \mathbf{r}_b}{2} \left[3 \frac{\mathbf{v}_b \cdot \mathbf{r}_b}{r_b^2} \mathbf{r}_b - 2 \mathbf{v}_b \right] \quad (\text{A.20})$$

A.6. Central Body Acceleration Term

The final term from the scalar potential is dependent on the acceleration \mathbf{a}_b of the central body:

$$w_{cba} = -\frac{\mu_b}{2c^2} \cdot \frac{\mathbf{a}_b \cdot \mathbf{r}_b}{r_b} \quad (\text{A.21})$$

Like before, we obtain the spacecraft's acceleration by taking the spatial derivative of w_{cba} :

$$\begin{aligned} \ddot{x}_{cba}^i &= -\frac{\mu_b}{2c^2} \left[\left(\frac{\partial}{\partial x^i} (\mathbf{a}_b \cdot \mathbf{r}_b) \right) \cdot \frac{1}{r_b} + \left(\frac{\partial}{\partial x^i} \frac{1}{r_b} \right) \cdot (\mathbf{a}_b \cdot \mathbf{r}_b) \right] \\ &= -\frac{\mu_b}{2c^2} \left[\frac{a_b^i}{r_b} - \frac{(\mathbf{a}_b \cdot \mathbf{r}_b) x^i}{r_b^3} \right] \end{aligned} \quad (\text{A.22})$$

Converting this to vector form yields:

$$\mathbf{a}_{cba} = \frac{\mu_b}{2r_b c^2} \left[\frac{\mathbf{a}_b \cdot \mathbf{r}_b}{r_b^2} \mathbf{r}_b - \mathbf{a}_b \right] \quad (\text{A.23})$$

A.7. Angular Momentum Term

The last two terms are derived from the vector potential w^i . First, we look at the term in Equation A.5 that includes the angular momentum \mathbf{S}_b of the central body:

$$w_{\text{ang}}^i = \frac{G(\mathbf{S}_b \times \mathbf{r}_b)^i}{2r_b^3} \quad (\text{A.24})$$

The acceleration caused by the central body's angular momentum is known as the Lense-Thirring effect. In our analysis, we make use of the Lense-Thirring acceleration term given by [26, p.155] (using the notation $\mathbf{J}_b = \frac{1}{M_b} \mathbf{S}_b$):

$$\mathbf{a}_{\text{ang}} = \frac{\mu_b}{r_b^3 c^2} \cdot (\gamma + 1) \left[\frac{3(\mathbf{r}_b \cdot \mathbf{J}_b)}{r_b^2} (\mathbf{r}_b \times \mathbf{v}) + \mathbf{v} \times \mathbf{J}_b \right] \quad (\text{A.25})$$

A.8. Extrinsic Gravitomagnetic Term

We call the second and final term in the vector potential the *extrinsic gravitomagnetic* term based on the common analogy between electromagnetism and relativistic gravity. Under this analogy, the angular momentum term derived above may also be called the *intrinsic gravitomagnetic* term (See e.g. [17]). The relevant potential term is:

$$w_{\text{xgm}}^i = w_0 v_b^i \quad \text{where} \quad w_0 = \frac{\mu_b}{r_b} \quad (\text{A.26})$$

Taking the spatial derivative of this potential we get:

$$w_{\text{xgm},j}^i = \mu_b v_b^i \frac{\partial}{\partial x^j} \left(\frac{1}{r_b} \right) = -\frac{\mu_b}{r_b^3} x^j v_b^i \quad (\text{A.27})$$

This derivative can then be used in the part of Equation A.8 pertaining to the vector potential:

$$\begin{aligned}
\dot{x}_{\text{xgm}}^i &= \frac{2(\gamma+1)}{c^2} \dot{x}^j \left(w_{\text{xgm},j}^i - w_{\text{xgm},i}^j \right) \\
&= \frac{2(\gamma+1)}{c^2} \left(\frac{\mu_b}{r_b^3} x^i v_b^j \dot{x}^j - \frac{\mu_b}{r_b^3} x^j v_b^i \dot{x}^j \right) \\
&= \frac{2(\gamma+1)\mu_b}{r_b^3 c^2} \left(v_b^j \dot{x}^j x^i - x^j \dot{x}^j v_b^i \right)
\end{aligned} \tag{A.28}$$

And finally, converting from tensor- to vector form, we get our expression for the extrinsic gravitomagnetic acceleration:

$$\mathbf{a}_{\text{xgm}} = \frac{\mu_b}{r_b^3 c^2} \cdot 2(\gamma+1) ((\mathbf{v}_b \cdot \mathbf{v}) \mathbf{r}_b - (\mathbf{r}_b \cdot \mathbf{v}) \mathbf{v}_b) \tag{A.29}$$

B

Model Verification

Carrying out our experimental simulations requires a functional software implementation of all the effects described in Section 2.3. Out of four light-time and six acceleration effects given, one of each (the Shapiro- and Schwarzschild terms) are fully implemented in Tudat. The remaining eight effects were added as part of this project, facilitated by Tudat's extensible design. Here we look at the methods used to validate our implementations. The dynamical- and observation effects are covered in Sections B.1 and B.2, respectively.

B.1. Acceleration Models

In total, six relativistic acceleration effects have been presented in Section 2.3.2. To verify that our software implementation of these models does what we expect it to, a simulation was carried out to observe the long-term behaviour of a Juno-like orbiter. The spacecraft was placed in an orbit similar to Juno's originally planned 14-day science orbit. The only difference between this orbit and that used in our experiment (See Table 2.4) is the apoapsis radius, which is lowered to 1.68×10^9 m. Additionally, the orbit is propagated for 12 years, between 10 November 2004 and the same date in 2016. The magnitudes of the six relativistic acceleration components were recorded, and can be found in Figure B.1.

There are a few notable features we can note in these plots that indicate that our software implementation was successful. First, the overall magnitudes of each effect is in agreement with the rough estimates made in Table 2.2. Because these estimates were conservative (i.e. large) we should expect the actual simulated values to be similar to or smaller than the estimates. This is indeed what we see in these results. Some effects, such as the Schwarzschild acceleration, are much smaller than their estimates due to their dependence on the geometry of the system. Additionally, we can see a frequent per-orbit oscillation in the acceleration magnitude, which we should expect from an elliptic orbit.

We can also identify some qualitative features that indicate the acceleration effects were implemented correctly. First, the kinetic- and external potential curves increase in magnitude slightly towards the middle of the year. We know that these two effects are proportional to one another with a factor of $v_b^2 r_{SJ} / c^2 \mu_S$. The two effects increase in magnitude as a result of Jupiter being closer to the Sun during a certain part of the year. Both Jupiter's speed and its gravitational potential w.r.t. the Sun increase during this period.

Similar annual and semi-annual signatures can be seen in the central body velocity- and extrinsic gravitomagnetic acceleration graphs. These are a result of the system's geometry, which periodically change to make certain terms small. Because our spacecraft is in a polar orbit, the velocity vector of Jupiter becomes perpendicular to Juno's orbital plane twice per Jovian year. This forces the factor $\mathbf{v}_b \cdot \mathbf{r}_b / 2$ in \mathbf{a}_{cbv} to zero, causing the two distinct minima. A similar phenomenon occurs with \mathbf{a}_{xgm} , where the spacecraft's and Jupiter's velocity vectors become perpendicular, i.e. $\mathbf{v}_b \cdot \mathbf{v} = 0$. Two less intense minima appear when \mathbf{v}_b becomes embedded within the spacecraft's orbital plane. During this period, \mathbf{r}_b and \mathbf{v}_b become aligned in opposing directions once per orbit, cancelling the two terms in \mathbf{a}_{xgm} .

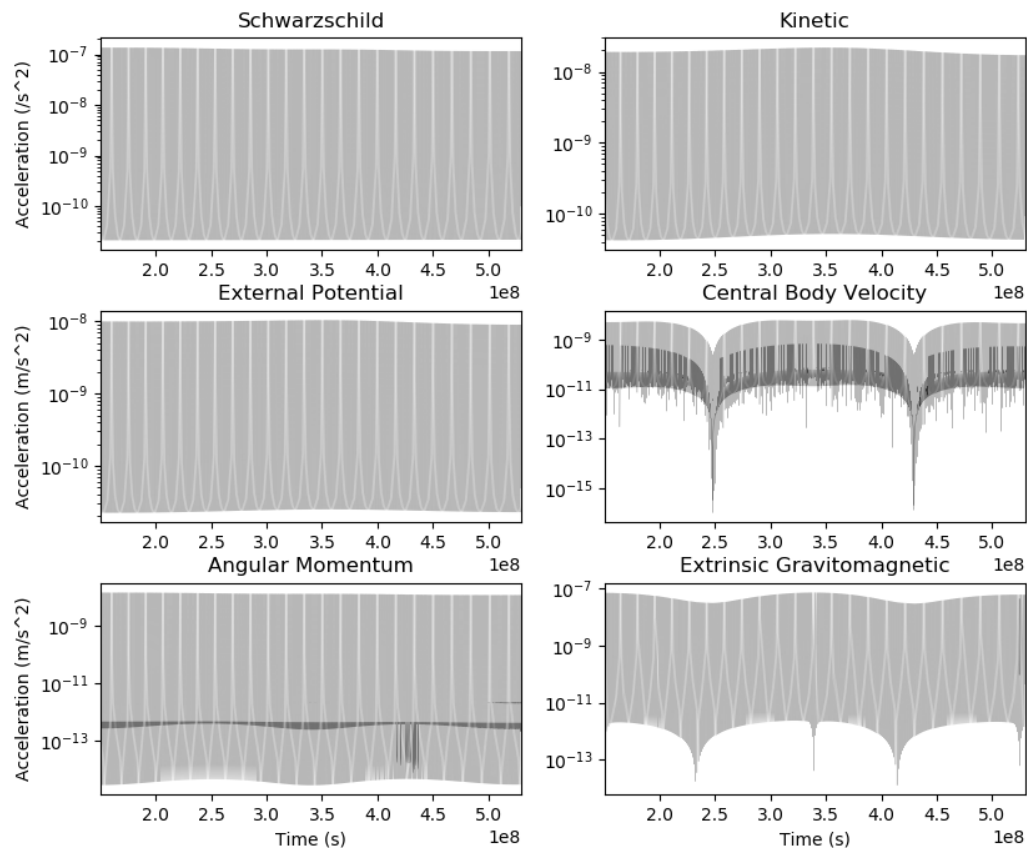


Figure B.1: Relativistic accelerations experienced by a Juno-like orbiter over the course of one Jovian year (≈ 12 years). Time is expressed in seconds after J2000.

B.2. Light Time Models

To verify our relativistic light time correction implementations, we use the data given by [12] as a reference and try to replicate it. A simulation similar to the one described above (Juno-like, 14-day polar orbit around Jupiter) was run for a period of 365 days. Light time observations and relativistic corrections were generated throughout this simulation period. While the initial conditions of the original paper were not replicated exactly, the results have sufficiently many qualitative and quantitative similarities to demonstrate that the two implementations are similar.

First, we can compare the relative magnitudes of the light time corrections between the two implementations. All four effects show agreement with respect to this criterion. The shapes of the curves for each effect also show clear similarities between the implementations, both with respect to per-orbit effects and the annual signal caused by Earth's orbit. For the velocity light time correction, a distinct long-term qualitative change in the shape of the per-orbit curve shape can be identified in both cases. Overall, interpret these similarities as an indication that our light time correction implementation is in agreement with that presented in [12].

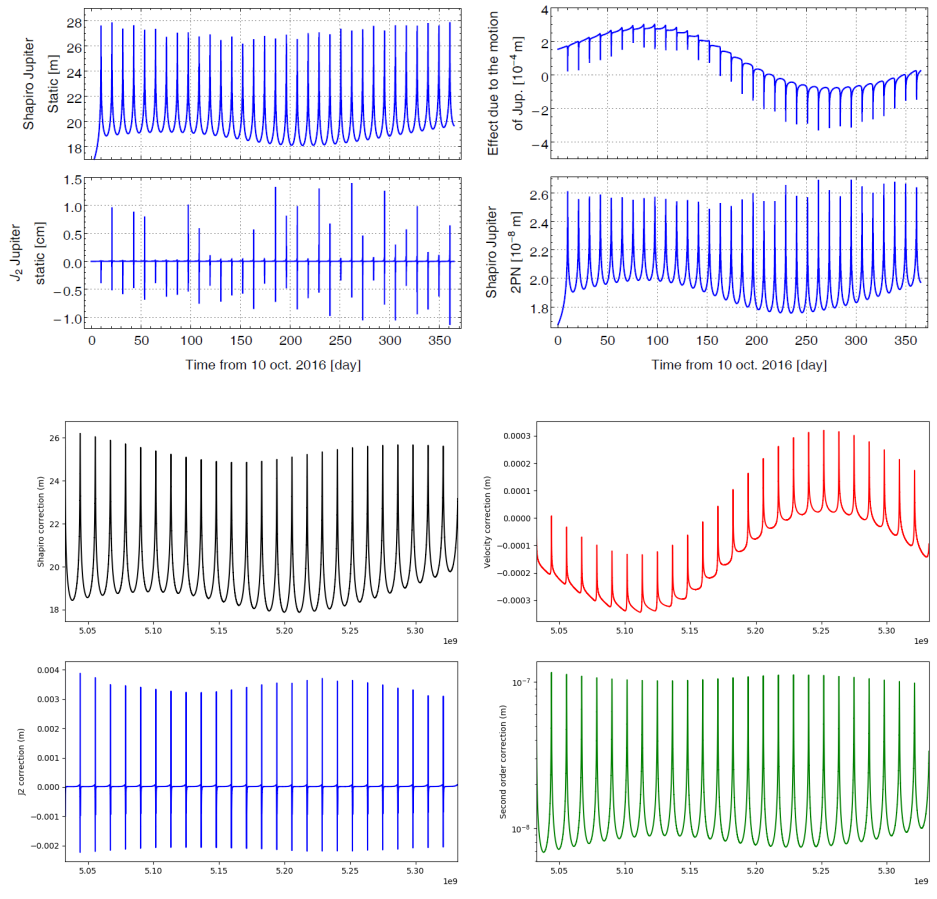
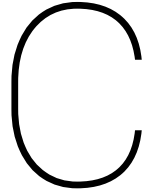


Figure B.2: Simulated relativistic light time corrections given in [12] (Top) and an approximate recreation using our software implementation (Bottom).



Integrator Benchmarking

As was mentioned in Section 2.4.2, the state and variational equations in our experiment were propagated using a Runge-Kutta seventh order integrator with a 10 s step size. In this appendix we describe the method used to make this choice, as well as evidence that the integrator's performance is sufficient.

C.1. Integrator Selection

The chosen integration scheme was selected based on the criterion that the total positional error at the end of an arc should not be large enough to significantly influence our results. Runge-Kutta integrators of fourth order (RK4) and seventh order (RK7) were considered initially, with the option left open to use more advanced integrator types if none of those tested fulfilled the criterion. An orbit integration was set up that is similar to that used in the final experiment (See Table 2.4). A simple environment with a spacecraft and Jupiter was created, with only point-mass gravity ($\mathbf{a} = -\mu\mathbf{r}/r^3$) being modelled. By using this simplified model, the numerically propagated spacecraft trajectory can be compared with an idealized Kepler orbit. Additionally, the integration period was doubled from 12 hours to 24 hours to allow for a margin of error.

The orbit of the spacecraft was propagated over a symmetric 24-hour period about the periapsis using RK4 and RK7 integrators with different step sizes between 0.5 and 50 seconds. The initial state was also propagated analytically according to an elliptical Kepler orbit to get a final reference state. The final distance between the analytically and numerically propagated states was recorded for each integrator type. Figure C.1 shows the results of the se simulations.

As we would expect, the RK7 integrators outperform RK4 for larger step sizes. The RK4 fall just within the desired error tolerance for step sizes of 0.5, 1 and 2 s. The final error of both RK4- and RK7 integrators for step sizes between 0.6 and 0.9 s is much larger than expected, on the order of 10 to 100 m. The cause of this discrepancy is unknown, though it may be caused by the rounding behaviour of the Tudat's Kepler orbit propagation method. Similar error can be seen for step sizes between 2 and 9 s. It appears that step sizes that are round numbers (0.5, 1, 10 s) result in lower final error figures. Out of the tested options, the RK7 integrator with 10 s step size was chosen for the experiment. Its final error falls within the prescribed criterion with an order of magnitude of margin. Its speed was also reasonable, making it feasible to run our simulations within a fairly short time (around 1 hour to run all 22 experiments).

C.2. Verification

To check that integrator error is not impacting our final results, we can look at the observation residuals (See Section 2.5.3) of the control experiment. For this parameter estimation run, where the truth- and estimation models are identical, we should expect the residuals to be normally distributed about zero. In fact, they should have the same distribution as the observation noise. If there are anomalies in this data, integration error could be a possible source.

Figure C.2 Shows the residual data of the final experiment's control run. There are around 6,000 samples, and they are indeed similarly distributed to the observation noise. The mean residual value of -8×10^{-6} indicates

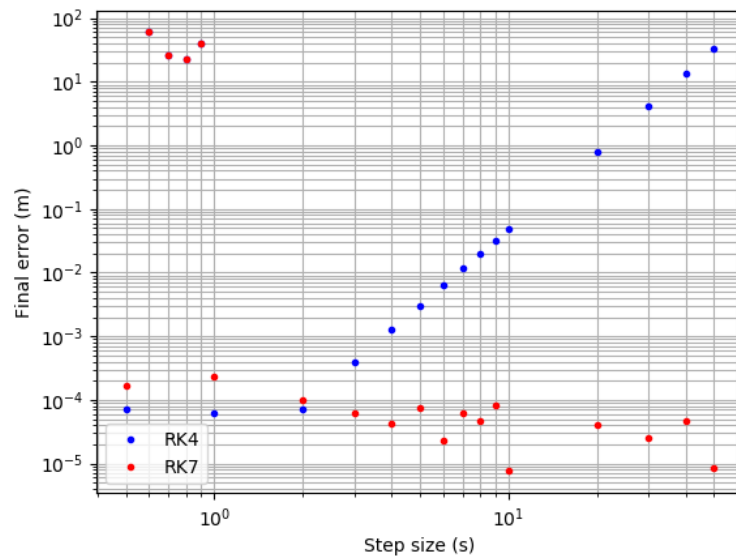


Figure C.1: Comparison of final error for Runge-Kutta integrators with different step sizes.

that the residuals are centered around zero, and the standard deviation of $1.004 \times 10^{-3} m$ is close to the actual noise level of 1 mm.

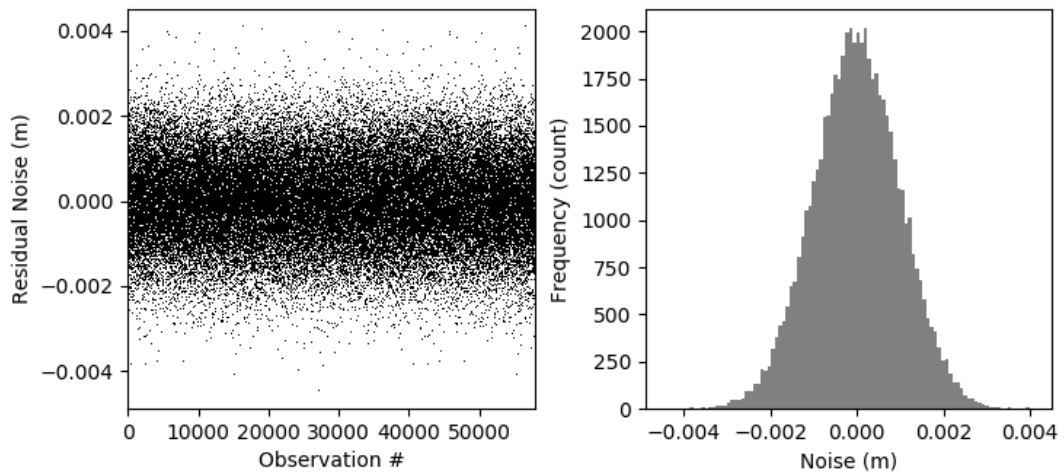


Figure C.2: Distribution of the control observation residuals.

Bibliography

- [1] Charles Acton. SPICE - an observation geometry system for space science missions. Web, May 2019. <https://naif.jpl.nasa.gov/naif/index.html>.
- [2] S. Bauer, H. Hussmann, J. Oberst, D. Dirx, D. Mao, G.A. Neumann, E. Mazarico, M. H. Torrence, J. F. McGarry, D. E. Smith, and M. T. Zuber. Analysis of one-way laser ranging data to LRO, time transfer and clock characterization. *Icarus*, 283, February 2017.
- [3] Sven Bauer. Application of one-way laser ranging data to the lunar reconnaissance orbiter (LRO) for time transfer, clock characterization and orbit determination. PhD Thesis, Technische Universität Berlin, 2017.
- [4] B. Bertotti, L. Iess, and P. Tortora. A test of general relativity using radio links with the cassini spacecraft. *Nature*, 425, September 2003.
- [5] Luc Blanchet, Christophe Salomon, Pierre Teyssandier, and Peter Wolf. Relativistic theory for time and frequency transfer to order c^{-3} . *Astronomy and Astrophysics*, 370, April 2001.
- [6] Dwayne Brown and Laurie Cantillo. Nasa's juno mission to remain in current orbit at jupiter. Press release, August 2017. <https://www.nasa.gov/press-release/nasa-s-juno-mission-to-remain-in-current-orbit-at-jupiter/>.
- [7] John J. Degnan. Asynchronous laser transponders for precise interplanetary ranging and time transfer. *Journal of Geodynamics*, 34, 2002.
- [8] D. Dirx, R. Noomen, P. N. A. M. Visser, L. Gurvits, and L. L. A. Vermeersen. Simultaneous spacetime dynamics estimation from space mission tracking data. *Astronomy and Astrophysics*, 587, December 2015.
- [9] D. Dirx, V. Lainey, L. I. Gurvits, and P. N. A. M. Visser. Dynamical modelling of the galilean moons for the JUICE mission. *Planetary and Space Science*, 134, December 2016.
- [10] Dominic Dirx, Ivan Prochazka, Sven Bauer, Pieter Visser, Ron Noomen, Leonid I. Gurvits, and Bert Vermeersen. Laser and radio tracking for planetary science missions - a comparison. *Journal of Geodesy*, July 2018.
- [11] James B. Hartle. *Gravity - An Introduction to Einstein's General Relativity*. Addison-Wesley, 2003.
- [12] A. Hees, S. Bertone, and C. Le Poncin-Lafitte. Light propagation in the field of a moving axisymmetric body: theory and application to juno. *Physical Review D*, 90, October 2014.
- [13] Luciano Iess, Mauro Di Benedetto, Nick James, Mattia Mercolino, Lorenzo Simone, and Paolo Tortora. Astra: Interdisciplinary study on enhancement of the end-to-end accuracy for spacecraft tracking techniques. *Acta Astronautica*, 94, February 2014.
- [14] Alex S. Konopliv, Sami W. Asmar, William M. Folkner, Özgür Karatekin, Danciel C. Nunes, Suzanne E. Smrekar, Charles F. Yoder, and Maria T. Zuber. Mars high resolution gravity fields from mro, mars seasonal gravity, and other dynamical parameters. *Icarus*, 211, 2011.
- [15] S. M. Kopeikin. The gravitomagnetic influence on earth-orbiting spacecrafts on the lunar orbit. *Astrophysics and Space Science Library*, 367, 2010.
- [16] Sergei Kopeikin, Michael Efroimsky, and George Kaplan. *Relativistic Celestial Mechanics of the Solar System*. Wiley-VCH, 2011.

- [17] Sergei M. Kopeikin. Gravitomagnetism and the speed of gravity. *Internanional Journal of Modern Physics D*, 15, March 2006.
- [18] Christophe le Poncin-Lafitte, Bernard Linet, and Pierre Teyssandier. World function and time transfer: general post-minkowskian expansions. *Classical and Quantum Gravity*, 21, 2004.
- [19] Jack J. Lissauer and Imke de Pater. *Fundamental Planetary Science - Physics, Chemistry and Habitability*. Cambridge University Press, 4 edition, 2017.
- [20] Charles W. Misner, Kip S. Thorne, and John Archibald Wheeler. *Gravitation*. W. H. Freeman and Company, 1973.
- [21] Oliver Montenbruck and Eberhard Gill. *Satellite Orbits - Models, Methods and Applications*. Springer, 2005.
- [22] T. W. Murphy. Lunar laser ranging: the millimeter challenge. *Reports on Progress in Physics*, 76, 2013.
- [23] Wei-Tou Ni. Theoretical framework for testing relativistic gravity. iv. a compendium of metric theories of gravity and their post-newtonian limits. *The Astrophysical Journal*, 176, September 1972.
- [24] Hirotomo Noda, Hiroo Kunimori, Takahide Mizuno, Hiroki Senshu, Naoko Ogawa, Hiroshi Takeuchi, Chris Moore, Alex Pollard, Tomohiro Yamaguchi, Noriyuki Namiki, Teiji Kase, Takano Saki, and Yuichi Tsuda. Laser link experiment with the hayabusa2 laser altimeter for in-flight alignment and measurement. *Earth, Planets and Space*, 69, 2017.
- [25] M. R. Pearlman, J. J. Degnan, and J. M. Bosworth. The international laser ranging service. *Advances in Space Research*, 30, 2002.
- [26] Gérard Petit and Brian Luzum. IERS conventions (2010). International Earth Rotation and Reference System Service, 2010.
- [27] I. I. Shapiro, R. D. Reasenberg, P. E. MacNeil, R. B. Goldstein, J. P. Brenkle, D. L. Cain, T. Komarek, A. Al. Zyguelbaum, W. F. Cuddihy, and W. H. Michael Jr. The viking relativity experiment. *Journal of Geophysical Research*, 82, September 1977.
- [28] Irwin I. Shapiro. Fourth test of general relativity. *Physical Review Letters*, 13, December 1964.
- [29] David E. Smith, Maria T. Zuber, Xiaoli Sun, Gregory A. Neumann, John F. Cavanaugh, Jan F. McGarry, and Thomas W. Zagwodzki. Two-way laser link over interplanetary distance. *Science*, 311, January 2006.
- [30] M. Soffel et al. The IAU 2000 Resolutions for Astrometry, Celestial Mechanics and Metrology in the Relativistic Framework: Explanatory Supplement. *The Astronomical Journal*, 126, December 2003.
- [31] J. L. Synge. A characteristic function in riemannian space and its application to the solution of geodesic triangles. *Proceedings of the London Mathematical Society*, 32, 1931.
- [32] Pierre Teyssandier and Christophe le Poncin-Lafitte. General post-Minkowskian expansion of time transfer functions. *Classical and Quantum Gravity*, 25, July 2008.
- [33] Catherine L. Thornton and James S. Border. *Radiometric Tracking Techniques for Deep-Space Navigation*. Deep-Space Communications and Navigation Series. Jet Propulsion Laboratory, California Institute of Technology, October 2000.
- [34] Slava G. Turyshev, William Farr, William M. Folkner, André R. Girerd, Hamid Hemmati, Thomas W. Murphy Jr., James G. Williams, and John J. Degnan. Advancing tests of relativistic gravity via laser ranging to phobos. *Experimental Astronomy*, 28, March 2010.
- [35] Clifford M. Will. Theoretical frameworks for testing relativistic gravity. ii. parametrized post-newtonian hydrodynamics, and the nordtvedt effect. *The Astrophysical Journal*, 163, February 1971.